End-to-end distribution for a wormlike chain in arbitrary dimensions

Shafigh Mehraeen,[1] Bariz Sudhanshu,[2] Elena F. Koslover,[3] and Andrew J. Spakowitz[2,3]
[1] *Department of Mechanical Engineering, Stanford University, Stanford, California 94305, USA*
[2] *Department of Chemical Engineering, Stanford University, Stanford, California 94305, USA*
[3] *Biophysics Program, Stanford University, Stanford, California 94305, USA*
(Received 25 July 2007; revised manuscript received 12 September 2007; published 9 June 2008)

We construct an efficient methodology for calculating wormlike chain statistics in arbitrary D dimensions over all chain rigidities, from fully rigid to completely flexible. The structure of our exact analytical solution for the end-to-end distribution function for a wormlike chain in arbitrary D dimensions in Fourier-Laplace space (i.e., Fourier-transformed end position and Laplace-transformed chain length) adopts the form of an infinite continued fraction, which is advantageous for its compact structure and stability for numerical implementation. We then proceed to present a step-by-step methodology for performing the Fourier-Laplace inversion in order to make full use of our results in general applications. Asymptotic methods for evaluating the Laplace inversion (power-law expansion and Rayleigh-Schrödinger perturbation theory) are employed in order to improve the accuracy of the numerical inversions of the end-to-end distribution function in real space. We adapt our results to the evaluation of the single-chain structure factor, rendering simple, closed-form expressions that facilitate comparison with scattering experiments. Using our techniques, the accuracy of the end-to-end distribution function is enhanced up to the limit of the machine precision. We demonstrate the utility of our methodology with realizations of the chain statistics, giving a general methodology that can be applied to a wide range of biophysical problems.

DOI: 10.1103/PhysRevE.77.061803 PACS number(s): 36.20.Ey, 05.20.−y, 87.15.−v

I. INTRODUCTION

Many biopolymers such as DNA, collagen, actin filaments, and microtubules have a molecular architecture that confers elastic rigidity to the resulting assembly. Therefore, understanding the impact of molecular rigidity on polymer behavior is necessary to address the physics that underlies a variety of biological processes. A polymer with intrinsic elasticity exhibits rigid behavior at small length scales, whereas it resembles a flexible chain at large length scales; such polymers are termed semiflexible. The simplest model for a semiflexible polymer is the wormlike chain model [1,2], which describes the chain as an inextensible thread with a linear-elastic bending energy [3,4] subjected to thermal fluctuations. The wormlike chain model acts as a fundamental tool to predict the physical behavior of many biopolymers, such as DNA [5,6].

In order to make use of the wormlike chain model in practical applications, it is necessary to have an accurate method of evaluating the governing chain statistics. However, there exist substantial mathematical challenges in calculating the chain statistics across the entire range of chain rigidities while enforcing the inextensibility constraint. The end-to-end distribution function is obtained approximately for nearly flexible polymers in the form of corrections to the Gaussian distribution function [7–11]. In the short-length or rigid-rod limit, the chain statistics are found using the path integral formalism in the WKB approximation including fixed end orientations [12] and by analytically evaluating the partition function by summing over transverse fluctuations about a nearly straight chain [13]. Relaxing the inextensibility constraint such that the chain length is globally fixed [14], the tangent magnitude is constrained at one end [15,16], or the tangent magnitude fluctuates about an average value [17–20] permits the evaluation of chain statistics that approximate the wormlike chain model. Other semiflexible-polymer models, such as the Dirac chain [21,22], are valuable in understanding the physical behavior of semiflexible polymers [23] and give qualitatively similar results to the wormlike chain model (for example, see Ref. [24] for a comparison between structure factors for the wormlike chain model and the Dirac chain).

Several works aim to evaluate wormlike chain statistics over the entire chain-rigidity spectrum. One approach provides a numerical solution by a direct diagonalization of the truncated scattering matrix [25,26]; this work unearths a striking double-peaked structure in the end-to-end distance distribution at intermediate chain rigidities. Exact results for the end-to-end distribution function in three dimensions in Fourier-Laplace space [11,27] (Fourier-transformed end position and Laplace-transformed chain length) are obtained using algebraic techniques developed for graph-theoretical problems involving regular planar lattices [28]. Exact results for wormlike chain statistics in two and three dimensions in Fourier-Laplace space are found to adopt the form of infinite continued fractions [24,29,30]; these solutions exploit diagrammatic methods from which the hierarchical structure of the continued fraction naturally emerges. The methodology behind these solutions renders exact results for a wormlike chain in two and three dimensions [24], subject to end-orientation constraint [29], and containing the influence of twist [30]. The statistical behavior of the wormlike chain model in real space requires an inversion from Fourier-Laplace space. Numerical methods to perform these inversions are not discussed in detail in Refs. [11,24–27,29,30]. An efficient numerical strategy for performing these inversions is necessary to achieve realizations of wormlike chain statistics with a desired accuracy.

Dimensionality plays an important role in understanding the effect of self-interaction on the physical size of a polymer chain [31,32]. Although practical applications of polymer theory are restricted to two (e.g., surface or spatial confinement) or three spatial dimensions, the physical behavior of a polymer embedded in arbitrary D dimensions is a necessary theoretical result that renders practical solutions that are felt in two and three dimensions. In the case of a flexible polymer, the noninteracting chain statistics obey a Gaussian distribution, regardless of the number of spatial dimensions. As such, the evaluation of the impact of self-interaction on the polymer size, either perturbatively [33,34] or via a renormalization group analysis [32,35], renders results that are analytically tractable and convenient to understand a variety of experimentally observed behaviors. Similarly, the size of a semiflexible polymer is impacted by the number of spatial dimensions within which it lives [36–42]. However, the treatment of self-interaction for a semiflexible polymer is complicated by the complexity inherent in the chain statistics. The wormlike chain model currently does not have an analytical solution for the chain statistics in arbitrary dimensions, which would facilitate the study of the impact of self-interaction on the size of a semiflexible polymer.

Our goal in this paper is to construct an efficient methodology for calculating accurate wormlike chain statistics over all chain rigidities in arbitrary D dimensions ($D \geq 1$, including partial dimensions). For the first time, we present an exact solution for the end-to-end distribution function for a wormlike chain in arbitrary D dimensions in Fourier-Laplace space with end-orientation constraint. Utilizing the exact and concise continued-fraction form of the end-to-end distribution function in Fourier-Laplace space, we introduce a step-by-step procedure for performing the Fourier-Laplace inversion. We also develop asymptotic results for the Laplace inversion that leverage expansion techniques, such as direct power-law expansion of the continued fractions and Rayleigh-Schrödinger perturbation theory. We then adapt our results to the evaluation of the single-chain structure factor, resulting in a simple, closed-form result that is amenable to direct comparison with scattering experiments. With our methodology in place, we achieve machine-precision accuracy for the end-to-end distribution function for a wormlike chain in real space and D dimensions. As such, our methods achieve a general utility in addressing problems involving semiflexible polymers in a variety of settings.

The outline of this paper is as follows. In Sec. II, we introduce the general wormlike chain end-to-end distribution function in D dimensions in Fourier-Laplace space. Next, a step-by-step methodology for achieving accurate inversion of the Fourier-Laplace transform is presented in Sec. III. The single-chain structure factor is presented in Sec. IV, giving a general methodology for evaluating the structure factor and asymptotic expressions that facilitate implementation. Section V illustrates the D-dimensional solution for the end-to-end distribution function and the utility of our inversion techniques. We provide a summary of our results in Sec. VI. In addition, the Appendix contains an accuracy-enhancement procedure for the partition function of a wormlike chain subjected to tension.

II. *D*-DIMENSIONAL GREEN FUNCTION

In this section, we derive the end-to-end distribution function or Green function for a wormlike chain in arbitrary D-dimensional space. The wormlike chain model in D dimensions is characterized by a D-dimensional space curve $\vec{r}(s)$, where the path-length coordinate s varies from zero at one chain end to the contour length L at the opposite end. The polymer chain is defined to be inextensible, which is imposed by constraining the tangent vector $\vec{u}(s) \equiv \partial_s \vec{r}$ to have unit magnitude for all values of s. The hyperspherical angles $\phi, \theta_1, \theta_2, \ldots, \theta_{D-2}$ give the orientation of the tangent vector, such that [43]

$$\begin{aligned} u_1 &= \sin\,\theta_{D-2} \sin\,\theta_{D-3} \cdots \sin\,\theta_2 \sin\,\theta_1 \sin\,\phi, \\ u_2 &= \sin\,\theta_{D-2} \sin\,\theta_{D-3} \cdots \sin\,\theta_2 \sin\,\theta_1 \cos\,\phi, \\ u_3 &= \sin\,\theta_{D-2} \sin\,\theta_{D-3} \cdots \sin\,\theta_2 \cos\,\theta_1, \\ &\vdots \\ u_{D-1} &= \sin\,\theta_{D-2} \cos\,\theta_{D-3}, \\ u_D &= \cos\,\theta_{D-2}. \end{aligned} \tag{1}$$

The bending deformation energy of the chain is a quadratic function of the curvature $\partial_s \vec{u}$ and is given by [2]

$$\beta \mathcal{H}_0 = \frac{l_p}{2} \int_0^L ds \left(\frac{\partial \vec{u}}{\partial s} \right)^2, \tag{2}$$

where l_p is the persistence length, and $\beta = 1/(k_B T)$. Previous treatments with varied dimensionality define the bending deformation energy with the coefficient $(D-1) l_p/4$ [44–46], which equals our value of $l_p/2$ in three dimensions ($D=3$). In this work, we choose the scaling coefficient to be independent of the number of dimensions D, thus l_p scales with a bending rigidity of the chain that is independent of dimensionality. Therefore, our results give the behavior of a chain with a fixed material rigidity as the number of dimensions is altered, with the intention of clearly demonstrating the impact of dimensionality on the behavior of a polymer chain with constant physical properties. We note that our choice of Hamiltonian renders a Kuhn length that depends on dimensionality, rather than a universal Kuhn length $b = 2 l_p$ as in treatments such as Refs. [44–46]. Our results are easily converted to the description used in Refs. [44–46] through the simple parameter change $l_p \to (D-1) l_p/2$.

In the absence of end-position constraint, the Green function is defined by

$$G_0(\vec{u}|\vec{u}_0; L) = \int_{\vec{u}(s=0)=\vec{u}_0}^{\vec{u}(s=L)=\vec{u}} \mathcal{D}[\vec{u}(s)] \exp\{-\beta \mathcal{H}_0[\vec{u}(s)]\}, \tag{3}$$

which is the conditional probability that a chain with length L has fixed initial and final orientations, given by $\vec{u}_0$ and $\vec{u}$, respectively. In Eq. (3), the Green function $G_0(\vec{u}|\vec{u}_0; L)$ is calculated by the D-dimensional path integration $\mathcal{D}[\vec{u}(s)]$ over all possible paths of the fluctuating field $\vec{u}(s)$ [47]. We solve the "Schrödinger" equation obtained from Eq. (3) [48],

leading to the Green function in D dimensions given by

$$G_0(\vec{u}|\vec{u}_0;L)=\sum_{\lambda;\boldsymbol{\mu}} Y^{(D)*}_{\lambda;\boldsymbol{\mu}}(\vec{u})Y^{(D)}_{\lambda;\boldsymbol{\mu}}(\vec{u}_0)C^D_\lambda(N), \tag{4}$$

where $C^D_\lambda(N)=\exp(-\epsilon^D_\lambda N)$, $N=L/(2l_p)$, $\epsilon^D_\lambda=\lambda(\lambda+D-2)$, and $Y^{(D)}_{\lambda;\boldsymbol{\mu}}$ are the hyperspherical harmonics [43]. Here, $\boldsymbol{\mu}$ is a vector consisting of eigenvalues $(\mu_1,\mu_2,\ldots,\mu_{D-2})$.

We now consider the end-to-end distribution function $G(\vec{R},\vec{u}|\vec{u}_0;L)$, which gives the probability that a chain that begins at the origin with initial orientation $\vec{u}_0$ will have end position $\vec{R}$ and final orientation $\vec{u}$. As an extension of Eq. (3), $G(\vec{R},\vec{u}|\vec{u}_0;L)$ is written as

$$G(\vec{R},\vec{u}|\vec{u}_0;L)=\int_{\vec{u}(s=0)=\vec{u}_0}^{\vec{u}(s=L)=\vec{u}}\mathcal{D}[\vec{u}(s)] \times\exp\{-\beta\mathcal{H}_0[\vec{u}(s)]\}\delta\left(\vec{R}-\int_0^L ds\vec{u}\right), \tag{5}$$

where δ is a Dirac delta function that restricts the path integration to those paths that satisfy the fixed end separation $\vec{R}$. The path integral formulation of the Green function is used to find the governing "Schrödinger" equation [48]

$$\left(\frac{\partial}{\partial L}-\frac{1}{2l_p}\tilde{\nabla}^2_D+\vec{u}\cdot\vec{\nabla}_R\right)G(\vec{R},\vec{u}|\vec{u}_0;L)=\delta(L)\delta(\vec{R})\delta(\vec{u}-\vec{u}_0), \tag{6}$$

where $\tilde{\nabla}^2_D$ is the D-dimensional angular Laplacian, and $\vec{\nabla}_R$ is the D-dimensional gradient operator.

Upon D-dimensional Fourier transforming from the variable $\vec{R}$ to the wave vector $\vec{k}$, our problem becomes that of a single wormlike chain with Hamiltonian

$$\beta\mathcal{H}=\beta\mathcal{H}_0+\beta\mathcal{H}_{\text{ext}}=\frac{l_p}{2}\int_0^L ds\left(\frac{\partial\vec{u}}{\partial s}\right)^2-i\vec{k}\cdot\int_0^L ds\vec{u}. \tag{7}$$

The external Hamiltonian $\beta\mathcal{H}_{ext}$ naturally emerges in the Fourier transform of the end-to-end distribution function $G(\vec{R},\vec{u}|\vec{u}_0;L)$ due to the end-position constraint. The corresponding Schrödinger equation in Fourier space is

$$\left(\frac{\partial}{\partial L}-\frac{1}{2l_p}\tilde{\nabla}^2_D-i\vec{k}\cdot\vec{u}\right)G(\vec{k},\vec{u}|\vec{u}_0;L)=\delta(L)\delta(\vec{u}-\vec{u}_0), \tag{8}$$

which demonstrates the direct correspondence between our problem and that of a rigid rotor in a dipole field. We proceed to solve the Green function utilizing the path integral representation; however, the Schrödinger equation will be useful in the next section.

Without loss of generality, we rotate our D-dimensional coordinate system so that $\vec{k}$ aligns with the x_D axis, upon which $\beta\mathcal{H}_{\text{ext}}=-ikR_D$, where $R_D=\int_0^L ds\cos\theta_{D-2}(s)$ is the end-to-end distance projected onto the x_D axis, and k is the magnitude of $\vec{k}$. This is explicitly performed by setting the tangent vector to $\vec{u}=\boldsymbol{\Gamma}\cdot\vec{u}'$ such that $\vec{k}\cdot\vec{u}=\vec{k}\cdot\boldsymbol{\Gamma}\cdot\vec{u}'=k\hat{x}_D\cdot\vec{u}'$. This operation resets the initial orientation from $\vec{u}$ to $\vec{u}'=\boldsymbol{\Gamma}^{-1}\cdot\vec{u}$ and the final orientation $\vec{u}_0$ to $\vec{u}'_0=\boldsymbol{\Gamma}^{-1}\cdot\vec{u}_0$. However, this transformation does not affect the Hamiltonian $\beta\mathcal{H}_0$, which is invariant under coordinate rotation.

The external Hamiltonian is treated as a perturbation to the ground-state behavior, governed by Eq. (4). As such, we write

$$G(\vec{K},\vec{u}|\vec{u}_0;L)=\langle\exp(iKR_D)\rangle^{\vec{u}'}_{\vec{u}'_0}=\sum_{n=0}^{\infty}\frac{(iK)^n}{n!}\langle R^n_D\rangle^{\vec{u}'}_{\vec{u}'_0}, \tag{9}$$

where $\langle\ldots\rangle^{\vec{u}'}_{\vec{u}'_0}$ indicates an average taken with respect to the ground-state Hamiltonian $\beta\mathcal{H}_0$ [Eq. (2)] with fixed initial and final orientations given by $\vec{u}'_0$ and $\vec{u}'$, respectively. All lengths in Eq. (9) are made dimensionless by $2l_p$, and we introduce the reduced Fourier variable $\vec{K}\equiv 2l_p\vec{k}$ $(K=|\vec{K}|)$.

The nth moment in the Green-function expansion is written as

$$\langle R^n_D\rangle^{\vec{u}'}_{\vec{u}'_0}=\left\langle\prod_{i=1}^n\int_0^N ds_i\cos\theta_{D-2}(s_i)\right\rangle^{\vec{u}'}_{\vec{u}'_0} =n!\left\langle\prod_{i=1}^n\int_0^{s_{i+1}}ds_i\cos\theta_{D-2}(s_i)\right\rangle^{\vec{u}'}_{\vec{u}'_0}, \tag{10}$$

where the factor $n!$ comes from the "time" ordering of the integrations, and $s_{n+1}=N=L/(2l_p)$. The second, time-ordered form of Eq. (10) facilitates evaluation by exploiting the Markovian nature of the tangent-vector statistics. Procedurally, we insert a ground-state propagator [Eq. (4)] between each successive factor of $\cos\theta_{D-2}(s_i)$ in the product and propagators from the initial orientation $\vec{u}'_0$ to $\cos\theta_{D-2}(s_1)$ and from $\cos\theta_{D-2}(s_n)$ to the final orientation $\vec{u}'$. Each propagator contains a sum over eigenvalue indices $\{\lambda_i;\boldsymbol{\mu}_i\}$ $(i\in[0,n])$; thus, we have $(n+1)$ λ indices and $(n+1)$ sets of $\boldsymbol{\mu}$ indices to sum over, one for each of the $(n+1)$ inserted propagators. Initial and final orientations are fixed, so we only integrate over the intermediate orientations $\vec{u}_j$ $(j\in[1,n])$. In so doing, we arrive at the nth-moment expression

$$\begin{aligned}\langle R^n_D\rangle^{\vec{u}'}_{\vec{u}'_0}=&\frac{n!}{\Omega_D}\sum_{\lambda_n;\boldsymbol{\mu}_\mathbf{n}}\cdots\sum_{\lambda_0;\boldsymbol{\mu}_\mathbf{0}}\\ &\times\left[\prod_{i=1}^n\int_0^{s_{i+1}}ds_iC^D_{\lambda_i}(s_{i+1}-s_i)\right]\\ &\times C^D_{\lambda_0}(s_1)Y^{(D)*}_{\lambda_n;\boldsymbol{\mu}_\mathbf{n}}(\vec{u}')\\ &\times\left[\prod_{j=1}^n\int d\vec{u}_jY^{(D)}_{\lambda_j;\boldsymbol{\mu}_\mathbf{j}}(\vec{u}_j)\cos\theta_{D-2_j}Y^{(D)*}_{\lambda_{j-1};\boldsymbol{\mu}_\mathbf{j-1}}(\vec{u}_j)\right]\\ &\times Y^{(D)}_{\lambda_0;\boldsymbol{\mu}_\mathbf{0}}(\vec{u}'_0),\end{aligned} \tag{11}$$

where $s_{n+1}=N$, and $\Omega_D=2\pi^{D/2}/\Gamma(D/2)$ is the solid angle in D dimensions (e.g., $\Omega_3=4\pi$).

The $(n+1)$ summations over λ indices and $\boldsymbol{\mu}$ indices select values of these indices that survive integration over the intermediate orientations. The selection rules arise from the perturbation of the hyperspherical harmonics by the $\cos\theta_{D-2}$

terms. The hyperspherical harmonics are constructed as a product of Gegenbauer polynomials [43]. Using properties of the Gegenbauer polynomials [43], we find the selection rules for the intermediate λ indices and $\boldsymbol{\mu}$ indices to be

$$\int d\vec{u} Y^{(D)*}_{\lambda;\boldsymbol{\mu}}(\vec{u})\cos\,\theta_{D-2} Y^{(D)}_{\lambda';\boldsymbol{\mu}'}(\vec{u}) = \delta_{\boldsymbol{\mu},\boldsymbol{\mu}'}(a^{\mu_1}_{\lambda+1}\delta_{\lambda+1,\lambda'} + a^{\mu_1}_{\lambda}\delta_{\lambda-1,\lambda'}), \tag{12}$$

where δ is the Kronecker delta, and $a^{\mu_1}_{\lambda} = [\frac{(\lambda-\mu_1)(\lambda+\mu_1+D-3)}{(2\lambda+D-2)(2\lambda+D-4)}]^{1/2}$. The selection rules and coefficients $a^{\mu_1}_{\lambda}$ are consistent with those found for two and three dimensions in Refs. [24,29].

The selection rules are inserted into Eq. (11), leading to equivalent sets of $\boldsymbol{\mu}$ indices and a set of λ indices that are selected based on the criteria that $\lambda_i = \lambda_{i-1} \pm 1$ and $\lambda_i \geq \mu_1$. A given set of λ indices can be plotted sequentially to give a jagged path that connects λ_0 to λ_n. Such a plot is the basis of a diagrammatic representation of our selection rules [24,29,30,48] that greatly simplifies our mathematical analysis. Equation (11) adopts a convolution structure for the variable N. We perform a Laplace transform from N to the Laplace variable p, arriving at the nth moment in Laplace space

$$\langle R^n_D \rangle^{\vec{u}'}_{\vec{u}'_0} = \frac{n!}{\Omega_D} \sum_{\lambda_n} \sum_{\lambda_0} \sum_{\boldsymbol{\mu}} Y^{(D)*}_{\lambda_n;\boldsymbol{\mu}}(\vec{u}') Y^{(D)}_{\lambda_0;\boldsymbol{\mu}}(\vec{u}'_0) \times \sum_{\text{paths}}^{\lambda_0 \to \lambda_n} P^{-1}_{\lambda_0} \prod_{i=1}^{n} a^{\mu_1}_{\lambda_i + t_i} P^{-1}_{\lambda_i}, \tag{13}$$

where $P_\lambda = p + \lambda(\lambda + D - 2)$, $t_i = 0$ if $\lambda_i = \lambda_{i-1} + 1$ for step up, and $t_i = 1$ if $\lambda_i = \lambda_{i-1} - 1$ for step down. The summation over paths implies a summation over all λ-index paths that connect λ_0 to λ_n such that all $\lambda_i = \lambda_{i-1} \pm 1$ and $\lambda_i \geq \mu_1$. We refer the reader to Refs. [24,29,30,48] for a detailed discussion of our diagrammatic representation and its use in evaluating the moments of the distribution.

Our development of the nth moment found in Eq. (13) is inserted into the Laplace transform of the Green function [Eq. (9)]. Using the diagrammatic representation outlined in the previous paragraph and discussed in Refs [24,29,30], the Green function is now reduced to the algebraic problem of finding all possible λ-index paths that connect the initial value λ_0 to the final value λ with fixed μ_1. The Green function is therefore given by

$$G(\vec{K}, \vec{u} | \vec{u}_0; p) = \frac{1}{\Omega_D} \sum_{\lambda} \sum_{\lambda_0} \sum_{\boldsymbol{\mu}} Y^{(D)*}_{\lambda;\boldsymbol{\mu}}(\vec{u}') Y^{(D)}_{\lambda_0;\boldsymbol{\mu}}(\vec{u}'_0) \mathcal{G}^{\mu_1}_{\lambda_0,\lambda}, \tag{14}$$

where $\mathcal{G}^{\mu_1}_{\lambda_0,\lambda}$ is the infinite sum of all diagrams that connect λ_0 to λ with a fixed value of μ_1.

We conclude our derivation by presenting the exact solution for $\mathcal{G}^{\mu_1}_{\lambda_0,\lambda}$ by exploiting our diagrammatic methods, as in results found in Refs. [24,29,30]. We define the infinite sum of diagrams $W^{\mu_1}_{\lambda}$ with equal initial and final λ indices and fixed μ_1 value for all diagrams. This is given by

$$W^{\mu_1}_{\lambda} = \frac{1}{(a^{\mu_1}_{\lambda} K)^2 w^{\mu_1(-)}_{\lambda-1} + P_\lambda + (a^{\mu_1}_{\lambda+1} K)^2 w^{\mu_1(+)}_{\lambda+1}}, \tag{15}$$

where $P_\lambda = p + \lambda(\lambda + D - 2)$, and $a^{\mu_1}_{\lambda} = [\frac{(\lambda-\mu_1)(\lambda+\mu_1+D-3)}{(2\lambda+D-2)(2\lambda+D-4)}]^{1/2}$. The partial summation $w^{\mu_1(+)}_{\lambda}$ represents the sum of all diagrams that start and end at the same value of λ with fixed value μ_1 and with all intermediate λ indices equal to or above λ. The term $w^{\mu_1(-)}_{\lambda}$ gives the sum of all diagrams that start and end at λ with all intermediate λ values equal to or below λ and greater than or equal to μ_1. A recursive relation for these partial summations is written in continued-fraction form as

$$w^{\mu_1(+)}_{\lambda} = \frac{1}{P_\lambda + (a^{\mu_1}_{\lambda+1} K)^2 w^{\mu_1(+)}_{\lambda+1}}, \quad \lambda \geq \mu_1,$$

$$w^{\mu_1(-)}_{\lambda} = \begin{cases} \dfrac{1}{P_\lambda + (a^{\mu_1}_{\lambda} K)^2 w^{\mu_1(-)}_{\lambda-1}}, & \lambda \geq \mu_1 + 1 \\ \dfrac{1}{P_\lambda}, & \lambda = \mu_1. \end{cases} \tag{16}$$

The final form of $\mathcal{G}^{\mu_1}_{\lambda_0,\lambda}$ is constructed from these partial summations, resulting in

$$\mathcal{G}^{\mu_1}_{\lambda_0,\lambda} = \begin{cases} W^{\mu_1}_{\lambda_0}, & \lambda_0 = \lambda \\ W^{\mu_1}_{\lambda_0} \prod_{n=1}^{|\lambda-\lambda_0|} iK a^{\mu_1}_{\lambda_0+n} w^{\mu_1(+)}_{\lambda_0+n}, & \lambda_0 < \lambda \\ W^{\mu_1}_{\lambda_0} \prod_{n=1}^{|\lambda-\lambda_0|} iK a^{\mu_1}_{\lambda_0+1-n} w^{\mu_1(-)}_{\lambda_0-n}, & \lambda_0 > \lambda. \end{cases} \tag{17}$$

Expressions found in Eqs. (14)–(17) complete the D-dimensional solution of the end-to-end distribution function with fixed initial and final orientations in Fourier-Laplace space for the wormlike chain model.

Our result for the end-to-end distribution is greatly simplified in cases where the end orientations are not constrained (i.e., free to rotate) by integrating Eq. (14) over $\vec{u}'_0$ and $\vec{u}'$. We note the property of the hyperspherical harmonics

$$\int d\vec{u} Y^{(D)}_{\lambda;\boldsymbol{\mu}}(\vec{u}) = \sqrt{\Omega_D}\delta_{\lambda,0}\delta_{\boldsymbol{\mu},\mathbf{0}}, \tag{18}$$

where $\mathbf{0} = (\underbrace{0,0,\ldots,0}_{D-2})$. Inserting this into Eq. (14) leads to the Green function

$$G(\vec{K}; p) = \cfrac{1}{P_0 + \cfrac{(a_1 K)^2}{P_1 + \cfrac{(a_2 K)^2}{P_2 + \cfrac{(a_3 K)^2}{\cdots}}}}, \tag{19}$$

where $\vec{K} = 2l_p\vec{k}$, K is the magnitude of $\vec{K}$, $P_\lambda = p + \lambda(\lambda + D - 2)$, and $a_\lambda = [\frac{\lambda(\lambda+D-3)}{(2\lambda+D-2)(2\lambda+D-4)}]^{1/2}$. We note that this exact solution produces identical results as those given in Ref. [24] for two- and three-dimensional solutions. The two-dimensional solution is realized by noting that $a_1 \to 1/\sqrt{2}$ and $a_{\lambda \geq 2} \to 1/\sqrt{4}$ in the limit $D \to 2$.

III. GREEN FUNCTION IN REAL SPACE

The Green function found in the previous section requires both a Fourier and Laplace inversion. The general procedure that we adopt for performing these inversions is as follows:

(1) The inverse Laplace transform is performed at a fixed K value using residue theorem.

(2) The Fourier inversion is found by numerically integrating over the Fourier variable K, performing the Laplace inversion at each step of the numerical integration.

This simple procedure is used in Refs. [29,30] to render accurate realizations of the chain statistics. In this section, we discuss the details of the inversion procedure, develop asymptotic expressions that significantly improve the accuracy of the inversion, and give guidelines for implementation of these methods into calculations. We focus on the inversion of Eq. (19), which renders the end-to-end distribution without orientation constraint; however, our methods are amenable to the evaluation of the full Green function including orientation constraint.

A. Laplace inversion

The inversion of the Laplace transform from p to the number of Kuhn segments N is performed using the residue theorem. For a fixed value of K, the poles are identified as p values that render the denominator of Eq. (19) equal to zero. Since the solution is written as an infinite continued fraction, there exist an infinite number of residues. These are simple poles, representing the eigenvalues of the governing Schrödinger equation in Fourier space [Eq. (8)].

We define the lth pole $\mathcal{E}_l(K)$, where the ordering is according to the magnitude of the real part at $K=0$ [i.e., $\mathrm{Re}(\mathcal{E}_0) > \mathrm{Re}(\mathcal{E}_1) > \ldots$]. For convenience, we define the reciprocal of the partial summations to be $j_\lambda^{(+)}=(w_\lambda^{0(+)})^{-1}$, leading to the Green function $G=(j_0^{(+)})^{-1}$. Therefore, the poles must satisfy $j_0^{(+)}(K;p)\to 0$ as $p\to\mathcal{E}_l$ for any l. With these definitions, the Laplace inversion is written as

$$G(K;N) = \sum_{l=0}^{\infty} \lim_{p\to\mathcal{E}_l} [(p-\mathcal{E}_l)G(K;p)\exp(pN)]$$
$$= \sum_{l=0}^{\infty} \frac{\exp(\mathcal{E}_l N)}{\partial_p j_0^{(+)}(K;\mathcal{E}_l)}. \quad (20)$$

As the contribution from each eigenvalue decays exponentially with N, the infinite summation can be truncated to a finite number of terms once the desired accuracy is attained.

Accurate inversion of the Laplace transform requires an accurate method of evaluating the eigenvalues $\mathcal{E}_l$ and an accurate evaluation of the denominator of the summand in Eq. (20). We proceed to discuss each task separately, identifying methods for efficient evaluation. To achieve accuracy for all K values, we divide the frequency spectrum into three regimes: small K, intermediate K, and large K. In Fig. 1, we plot the eigenvalues $\mathcal{E}_l$ $(l=0,1,\ldots,5)$ versus the Fourier variable K for $D=3$ and $\mu_1=0$; the real and imaginary parts of $\mathcal{E}_l$ are shown in panels A and B, respectively. Figure 1 includes our three methods of evaluating $\mathcal{E}_l$, and we refer to this figure throughout this section to illustrate the valid range for each method.

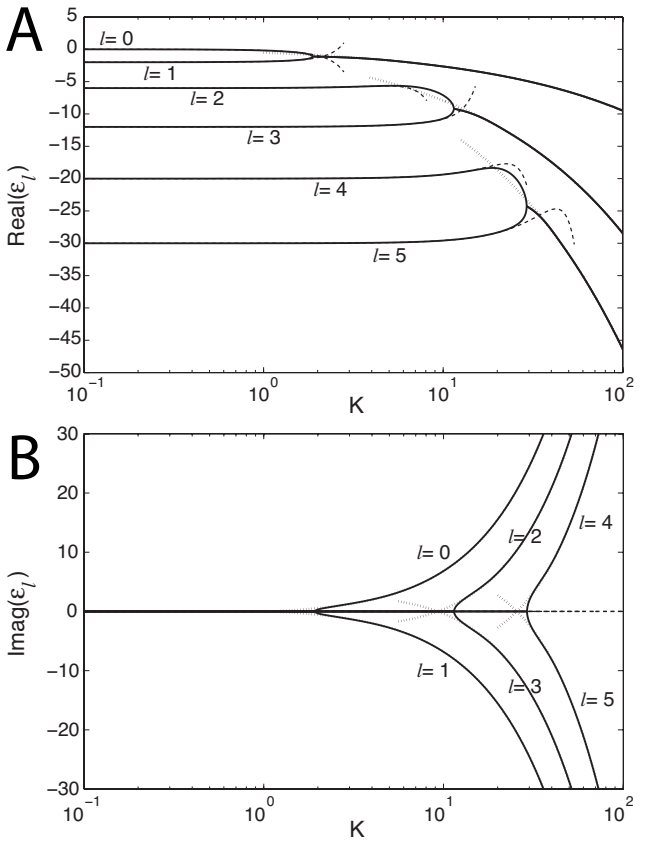

FIG. 1. Plots of the eigenvalues $\mathcal{E}_l$ for $l=0,1,\ldots,5$ vs the Fourier variable K for three dimensions $(D=3)$ and $\mu_1=0$. Panels A and B show the real and imaginary parts of $\mathcal{E}_l$, respectively. Three methods are employed to evaluate $\mathcal{E}_l$: small-K asymptotic expansion (dashed curve), intermediate-K matrix method (solid curve), and large-K asymptotic expansion (dotted curve).

1. Eigenvalue evaluation (small-K regime)

In the small-K regime, the eigenvalues $\mathcal{E}_l$ are accurately captured by a power-law expansion in powers of K^2. This natural form is consistent with the asymptotic behavior of the oblate spheroidal harmonics [49] that are closely related to the mathematical structure of our problem. The eigenvalues $\mathcal{E}_l$ satisfy $j_0^{(+)}=0$, which are used to find the Green function G [Eq. (19)]. The general Green function [Eq. (14)] includes terms with $\mu_1\neq 0$. For the sake of generality, we include $\mu_1\neq 0$ in our discussion of the small-K asymptotic behavior; however, evaluation of the Green function G [Eq. (19)] only includes $\mu_1=0$ as a contributor. Using recursion relations found in the previous section, we write that $\mathcal{E}_l$ satisfies

$$\mathcal{E}_l = -\epsilon_l^D - \frac{(a_l^{\mu_1}K)^2}{\epsilon_{l-1}^D + \mathcal{E}_l + \frac{(a_{l-1}^{\mu_1}K)^2}{\epsilon_{l-2}^D+\mathcal{E}_l+\frac{(a_{l-2}^{\mu_1}K)^2}{\cdots}}} - \frac{(a_{l+1}^{\mu_1}K)^2}{\epsilon_{l+1}^D + \mathcal{E}_l + \frac{(a_{l+2}^{\mu_1}K)^2}{\epsilon_{l+2}^D+\mathcal{E}_l+\frac{(a_{l+3}^{\mu_1}K)^2}{\cdots}}}, \tag{21}$$

where $\epsilon_l^D = l(l+D-2)$ and $a_l^{\mu_1} = \left[\frac{(l-\mu_1)(l+\mu_1+D-3)}{(2l+D-2)(2l+D-4)}\right]^{1/2}$. We note that since $a_{\mu_1}^{\mu_1}=0$, the first continued fraction in Eq. (21) truncates at the $\epsilon_{\mu_1}^D$ level.

The mathematical structure found in Eq. (21) permits an expansion of $\mathcal{E}_l$ in powers of K^2, i.e., $\mathcal{E}_l = \Sigma_{n=0}^{\infty} b_{2n}^{(l)} K^{2n}$, where $b_{2n}^{(l)}$ depends on the number of dimensions D. Truncation of this expansion yields an approximation for $\mathcal{E}_l$ in the small-K limit. The expansion coefficients $b_{2n}^{(l)}$ are found by expanding $\mathcal{E}_l$ in Eq. (21) and equating like powers of K. Following this procedure, the first three coefficients for general D and μ_1 and the first four coefficients for three dimensions are given in Table I. The coefficients in this expansion are all real; therefore, the small-K asymptotic expansion always predicts real eigenvalues. However, the eigenvalues $\mathcal{E}_l$ become complex with increasing K, as shown in Fig. 1, illustrating the need to transition from the small-K asymptote with increasing K.

2. Eigenvalue evaluation (intermediate-K regime)

With increasing K, adjacent eigenvalues ($\mathcal{E}_{2l}$ and $\mathcal{E}_{2l+1}$) converge to the same value on the real axis, then split into the complex plane such that $\mathcal{E}_{2l+1}=\mathcal{E}_{2l}^*$ for larger K (see Fig. 1). As such, eigenvalues at intermediate K cannot be accurately determined using the small-K asymptotic expansion. Thus, we employ a numerical method to calculate the eigenvalues that achieves accuracy for intermediate K values.

The infinite continued fraction form of the Green function is equivalently written as the first element of the inversion of an infinite tridiagonal matrix $\mathbf{J}=\mathbf{J}^{(0)}+p\mathbf{I}$ [50] (i.e., $G=J_{1,1}^{-1}$), where $\mathbf{I}$ is the infinite identity matrix. The diagonal elements of $\mathbf{J}^{(0)}$ are $J_{j,j}^{(0)}=\epsilon_{j-1}^D$ $(j=1,2,\ldots)$, and the off-diagonal elements are $J_{j,j+1}^{(0)}=J_{j+1,j}^{(0)}=-ia_jK$, where $\epsilon_j^D=j(j+D-2)$ and $a_j=a_j^0=\left[\frac{j(j+D-3)}{(2j+D-2)(2j+D-4)}\right]^{1/2}$. The eigenvalues $\mathcal{E}_l$ that we seek are given by the eigenvalues of the matrix $-\mathbf{J}^{(0)}$ [50]. This matrix transformation demonstrates the correspondence between our results and results for the wormlike chain Green function by a direct diagonalization of the truncated scattering matrix [26] and by graph-theoretic techniques [27].

The inversion of the general Green function [Eq. (14)] involves instances where $\mu_1\neq 0$. Extending the intermediate-K matrix method to the case $\mu_1\neq 0$ requires a redefinition of $\mathbf{J}^{(0)}$. The diagonal elements of $\mathbf{J}^{(0)}$ for $\mu_1\neq 0$ are $J_{j,j}^{(0)}=\epsilon_{\mu_1+j-1}^D$ $(j=1,2,\ldots)$, and the off-diagonal elements are $J_{j,j+1}^{(0)}=J_{j+1,j}^{(0)}=-ia_{\mu_1+j}^{\mu_1}K$, where $\epsilon_j^D=j(j+D-2)$ and $a_j^{\mu_1}=\left[\frac{(j-\mu_1)(j+\mu_1+D-3)}{(2j+D-2)(2j+D-4)}\right]^{1/2}$.

Truncation of the $\mathbf{J}$ matrix to a finite rank n_{cutoff} is equivalent to truncation of the infinite continued fraction at a finite level n_{cutoff}. Owing to the convergence properties of the continued fraction, sufficient accuracy is achieved upon truncation at a finite level. In practice, accurate calculation of the first n eigenvalues is achieved by choosing $n_{\text{cutoff}}=4n$.

TABLE I. Small-K asymptotic expansion coefficients for $\mathcal{E}_l$.

General D and μ_1

$$b_0^{(l)} = -l(l+D-2)$$

$$b_2^{(l)} = \frac{(a_l^{\mu_1})^2}{2l+D-3} - \frac{(a_{l+1}^{\mu_1})^2}{2l+D-1}$$

$$b_4^{(l)} = \frac{(a_l^{\mu_1})^4}{(2l+D-3)^3} - \frac{(a_{l+1}^{\mu_1})^4}{(2l+D-1)^3} + \frac{(a_{l+1}^{\mu_1}a_{l+2}^{\mu_1})^2}{2(2l+D)(2l+D-1)^2} - \frac{(a_l^{\mu_1}a_{l-1}^{\mu_1})^2}{2(2l+D-4)(2l+D-3)^2} - \frac{2(a_l^{\mu_1}a_{l+1}^{\mu_1})^2}{(2l+D-1)^2(2l+D-3)^2}$$

$D=3$, $\mu_1=0$

$$b_0^{(l)} = -l(l+1)$$

$$b_2^{(l)} = -\frac{1}{6-8l-8l^2}$$

$$b_4^{(l)} = -\frac{33+20l+20l^2}{8(-15+4l+4l^2)(-3+4l+4l^2)^3}$$

$$b_6^{(l)} = \frac{705+1000l+1144l^2+288l^3+144l^4}{4(-3+4l+4l^2)^5(525-200l-184l^2+32l^3+16l^4)}$$

3. Eigenvalue evaluation (large-K regime)

The intermediate-K matrix method does not accurately predict $\mathcal{E}_l$ for both very small K values and very large K values due to numerical challenges associated with finding the eigenvalues of a poorly balanced matrix. The small-K limit is effectively handled by the small-K expansion. Rayleigh-Schrödinger perturbation theory [51] is employed to obtain the asymptotic behavior of the eigenvalues of a rigid rotor in a dipole field in the limit of large field strength in three dimensions. Owing to the analogy between our problem and that of a rigid rotor, we employ a similar strategy to find the eigenvalue $\mathcal{E}_l$ in the large-K limit. In this section, we provide the large-K asymptotic expansion found using Rayleigh-Schrödinger perturbation theory. For completeness, we provide solutions including $\mu_1\neq 0$, despite the fact that $\mu_1=0$ for the Green function under consideration [Eq. (19)].

The Schrödinger equation found in Eq. (8) implies that our eigenvalues $\mathcal{E}_l$ satisfy

$$(\tilde{\nabla}_D^2 + iK\cos\theta_{D-2})\psi_l = \mathcal{E}_l\psi_l, \tag{22}$$

where ψ_l and $\mathcal{E}_l$ are eigenfunctions and eigenvalues of Eq. (8), respectively. The angular Laplacian $\tilde{\nabla}_D^2$ obeys the recursive relationship

$$\tilde{\nabla}_D^2 = \frac{\partial^2}{\partial\theta_{D-2}^2} + (D-2)\cot\theta_{D-2}\frac{\partial}{\partial\theta_{D-2}} + \frac{1}{\sin^2\theta_{D-2}}\tilde{\nabla}_{D-1}^2, \tag{23}$$

and operates on the hyperspherical harmonics such that $\tilde{\nabla}_{D-j}^2 Y_{l;\boldsymbol{\mu}}^{(D)} = -\mu_j(\mu_j+D-j-2)Y_{l;\boldsymbol{\mu}}^{(D)}$ for $j=0,1,\ldots,D-3$ and $\mu_0=l$ [43].

We adapt the perturbation procedure found in Ref. [51] to the large-K behavior of Eq. (22); we briefly outline the procedure as there exist nontrivial distinctions between the D-dimensional rigid rotor in an imaginary dipole field and the quantum mechanical rigid rotor in three dimensions

found in Ref. [51]. The eigenfunction ψ_l is expressed as $\psi_l = \sin^{\mu_1}\theta_{D-2}\Phi_l(\theta_{D-2})Y^{(D-1)}_{\mu_1,\mu_2,\ldots,\mu_{D-2}}(\phi,\theta_1,\ldots,\theta_{D-3})$, where $Y^{(D-1)}_{\mu_1,\mu_2,\ldots,\mu_{D-2}}(\phi,\theta_1,\ldots,\theta_{D-3})$ is the hyperspherical harmonic in $D-1$ dimensions (eigenvalues $\mu_1,\mu_2,\ldots,\mu_{D-2}$), and $\Phi_l(\theta_{D-2})$ is a currently unspecified function of θ_{D-2}. We define the perturbation parameter $\alpha=1/\sqrt{8K}$ and the variable $x=\alpha^{-1}\sin^2(\theta_{D-2}/2)$, with a range from zero to $\sqrt{8K}$, which approaches infinity as $K\to\infty$. Using these transformations and definitions in Eq. (8) and using Eq. (23), we now have the effective eigenvalue problem

$$(\mathcal{H}_0+\alpha\mathcal{H}')\Phi_l=\eta_l\Phi_l, \tag{24}$$

where the effective eigenvalue η_l is related to the original eigenvalue $\mathcal{E}_l$ according to

$$\mathcal{E}_l=iK-\mu_1(\mu_1+D-2)-\frac{1}{\alpha}\eta_l. \tag{25}$$

The effective Hamiltonian operator is split into the ground state $\mathcal{H}_0=-x\frac{d^2}{dx^2}-(\mu_1+1+\frac{D-3}{2})\frac{d}{dx}+\frac{x}{4}i$ and the perturbation $\mathcal{H}'=x^2\frac{d^2}{dx^2}+2(\mu_1+1+\frac{D-3}{2})x\frac{d}{dx}$.

This formulation makes it convenient to use Rayleigh-Schrödinger perturbation theory to find the eigenfunctions Φ_l and eigenvalues η_l [51]. The natural basis functions for $\mathcal{H}_0$ are the associated Laguerre functions, which are evaluated with argument x. The perturbing Hamiltonian $\mathcal{H}'$ is split into Hermitian and anti-Hermitian components, which renders a perturbed eigenfunction Φ_l with Hermitian and anti-Hermitian components. In the large-K limit, the eigenvalues $\mathcal{E}_l$ are complex (see Fig. 1) such that adjacent eigenvalues are complex conjugates, i.e., $\mathcal{E}_{2l+1}=\mathcal{E}^*_{2l}$. The eigenvalues found from the current formulation represent the even set, and the odd family is found as the complex conjugate of the even family.

Despite these complications, the perturbation procedure readily renders an expansion of Φ_l and η_l in powers of α. Following this procedure, we find the even eigenvalues $\mathcal{E}_{2l}$ adopt the form

$$\mathcal{E}_{2l}=iK-\mu_1(\mu_1+D-2)-\frac{1}{\alpha}\sum_{n=0}^{\infty}E_n^{(l)}\alpha^n, \tag{26}$$

where $\alpha=1/\sqrt{8K}$. The odd eigenvalues are found using $\mathcal{E}_{2l+1}=\mathcal{E}^*_{2l}$. Table II contains the large-K expansion coefficients $E_n^{(l)}$ up to $n=5$ (order K^{-2} contribution to $\mathcal{E}_{2l}$).

4. Implementation of the eigenvalue evaluation

The three methods for evaluating $\mathcal{E}_l$ provide a methodology for accurate and simple evaluation of the eigenvalues for determination of the wormlike chain Green function in arbitrary D dimensions. In Fig. 1, we provide plots of the real and imaginary components of $\mathcal{E}_l$ for $l=0,1,\ldots,5$ against the Fourier variable K. This plot includes the small-K asymptotic expansion (dashed curve), intermediate-K matrix method (solid curve), and large-K asymptotic expansion (dotted curve) for evaluating $\mathcal{E}_l$.

The behavior in Fig. 1 demonstrates two distinct regions for adjacent eigenvalues $\mathcal{E}_{2l}$ and $\mathcal{E}_{2l+1}$. For small-K, $\mathcal{E}_{2l}$ and $\mathcal{E}_{2l+1}$ are real valued and have distinctly separate values. At some critical value $K_l^{(c)}$, the adjacent eigenvalues merge their real components and split into the complex plane such that $\mathcal{E}_{2l+1}=\mathcal{E}^*_{2l}$. The small-$K$ asymptote accurately captures $\mathcal{E}_{2l}$ and $\mathcal{E}_{2l+1}$ up to K values just below $K_l^{(c)}$; the large-K asymptote converges with the eigenvalues just after the merger at $K_l^{(c)}$. It is necessary to utilize the intermediate-K matrix method only very near $K_l^{(c)}$. However, we find that the matrix method is sufficiently efficient and accurate in determining the eigenvalues for both small and intermediate K. Therefore, we opt to use the matrix method over the small-K asymptote on our calculations. On the other hand, the intermediate-K matrix method does not accurately predict the eigenvalues in the large-K limit; thus, the large-K asymptotic forms are critical in achieving both accuracy and efficiency in calculating the Green function.

TABLE II. Large-K asymptotic expansion coefficients for $\mathcal{E}_{2l}$.

In these expressions: $m=\mu_1+\frac{D-3}{2}$; $s=2l+m+1$; $l=0,1,2,3,\ldots$

$E_0^{(l)}=\left(\frac{1}{2\sqrt{2}}+\frac{i}{2\sqrt{2}}\right)s$

$E_1^{(l)}=-\frac{1}{8}(s^2+3-3m^2)-m(m+1)$

$E_2^{(l)}=\left(-\frac{1}{32\sqrt{2}}+\frac{i}{32\sqrt{2}}\right)s(s^2+3-9m^2)$

$E_3^{(l)}=\frac{i}{256}[(5s^4+34s^2+9)-(102s^2+42)m^2+33m^4]$

$E_4^{(l)}=\left(\frac{1}{2048\sqrt{2}}+\frac{i}{2048\sqrt{2}}\right)s[(33s^4+410s^2+405)-(1230s^2+1722)m^2+813m^4]$

$E_5^{(l)}=\frac{9}{4096}[(7s^6+140s^4+327s^2+54)-(420s^4+1350s^2+286)m^2+(495s^2+314)m^4-82m^6]$

5. Summand evaluation (small-K regime)

The summand in Eq. (20) is evaluated either by utilizing the continued fraction form of the Green function or through a perturbation expansion based on the Schrödinger equation [Eq. (22)]. The latter is particularly useful in the small-K limit due to balancing issues that arise in the evaluation of the continued fraction for small values of K. The l summand in the Laplace inversion [Eq. (20)] is related to the eigenfunction ψ_l satisfying Eq. (22) through the relationship

$$\frac{1}{\lim_{p\to\mathcal{E}_l}[\partial_p j_0^{(+)}]}=\left(\int d\vec{u}\,Y^{(D)*}_{0;\mathbf{0}}(\vec{u})\psi_l(\vec{u})\right)^2. \tag{27}$$

Rayleigh-Schrödinger perturbation theory provides the perturbed eigenvalues and the perturbed coefficients of the basis-set eigenfunctions. For $K=0$, the natural basis functions of Eq. (22) are the hyperspherical harmonics, thus corrections are found perturbatively from this basis. We perform the perturbation expansion and perform the angle integration to extract the summand for Eq. (20), resulting in the lowest-order expression

$$\frac{1}{\lim_{p\to\mathcal{E}_l}[\partial_p j_0^{(+)}]} \approx \begin{cases} 1, & l=0 \\ (-1)^l K^{2l} \prod_{j=0}^{l-1} \dfrac{a_{j+1}^2}{[l(l+1)-j(j+1)]^2}, & l \geq 1, \end{cases} \tag{28}$$

where $a_j=[\frac{j(j+D-3)}{(2j+D-2)(2j+D-4)}]^{1/2}$. This small-$K$ asymptotic form gives the lowest-order contribution for the $\mathcal{E}_l$ summand, which scales as K^{2l}. The next-order correction scales as K^{2l+2}.

For general problems with end constraints, it is necessary to Laplace invert $\mathcal{G}^{\mu_1}_{\lambda_0,\lambda}$ [Eq. (17)]. Our small-K asymptotic analysis is extended to perform this inversion in order to achieve numerical accuracy in this limit. From the Rayleigh-Schrödinger perturbation theory, the projection of the $\lambda,\boldsymbol{\mu}$ hyperspherical harmonic onto the lth eigenfunction of Eq. (22) (i.e., ψ_l) is given by

$$\mathcal{C}^{\mu_1}_{\lambda,l} = \int d\vec{u} Y^{(D)*}_{\lambda;\boldsymbol{\mu}}(\vec{u}) \psi_l(\vec{u}) \approx \begin{cases} 1, & \lambda = l \\ (-iK)^{l-\lambda} \prod_{j=\lambda}^{l-1} \dfrac{a^{\mu_1}_{j+1}}{l(l+1)-j(j+1)}, & l > \lambda \\ (-iK)^{\lambda-l} \prod_{j=l+1}^{\lambda} \dfrac{a^{\mu_1}_{j}}{l(l+1)-j(j+1)}, & l < \lambda. \end{cases} \tag{29}$$

With this in place, the Laplace inversion of $\mathcal{G}^{\mu_1}_{\lambda_0,\lambda}$ is found through the limit

$$\lim_{p\to\mathcal{E}_l}[(p-\mathcal{E}_l)\mathcal{G}^{\mu_1}_{\lambda_0,\lambda}(K;p)] \approx \mathcal{C}^{\mu_1}_{\lambda_0,l}\mathcal{C}^{\mu_1}_{\lambda,l}, \tag{30}$$

which gives the lowest-order approximation in K. This asymptotic result reduces to Eq. (28) for $\lambda_0=\lambda=\mu_1=0$.

6. Summand evaluation (continued-fraction method)

In the intermediate- and large-K regimes, the summand is accurately evaluated using the continued-fraction representation of the Green function [Eq. (19)]. We define a recursive representation for $j_n^{(+)}$ as

$$j_n^{(+)} = P_n + \frac{(a_{n+1}K)^2}{j_{n+1}^{(+)}}, \tag{31}$$

where $P_n=p+n(n+D-2)$, and $a_n=[\frac{n(n+D-3)}{(2n+D-2)(2n+D-4)}]^{1/2}$. The derivative of $j_n^{(+)}$ gives the recursion relation

$$\partial_p j_n^{(+)} = 1 - \frac{(a_{n+1}K)^2}{j_{n+1}^{(+)2}} \partial_p j_{n+1}^{(+)}. \tag{32}$$

These recursion expressions are useful for evaluating the continued fractions for small K values ($K<1$). These expressions are rebalanced for large K ($K\geq 1$) by defining $\tilde{j}_n^{(+)}=j_n^{(+)}/K$, leading to recursion relations that are better behaved numerically. Utilizing these recursion expressions to evaluate the summand in Eq. (20) requires truncation of the continued fraction at a cutoff n_{cutoff}, seeding the recursion with $j_{n_{\text{cutoff}}}^{(+)}=P_{n_{\text{cutoff}}}$ and $\partial_p j_{n_{\text{cutoff}}}^{(+)}=1$, and proceeding to cycle through the recursion expressions until $n=0$.

B. Fourier inversion

Once an efficient method for Laplace inversion is established, the Fourier transform must also be inverted. The Fourier inversion of the Green function is written as

$$G(\vec{R};N) = \frac{1}{(2\pi)^D}\int d\vec{k}\, \exp(-i\vec{k}\cdot\vec{R}) G(K;N) = \frac{1}{(2l_p)^D}\frac{1}{(2\pi)^{D/2}}\int_0^\infty dK K^{D-1}\frac{J_{D/2-1}(NrK)}{(NrK)^{D/2-1}} G(K;N), \tag{33}$$

where $\vec{K}=2l_p\vec{k}$ ($K=|\vec{K}|$), $\vec{r}=\vec{R}/L$ ($r=|\vec{r}|$), and $J_n(z)$ is the Bessel function of the first kind.

Integration over K is performed numerically from $K=0$ to $K=K_{\text{cutoff}}$, where K_{cutoff} is a cutoff value that is sufficiently large to achieve convergence. The K-step size in the numerical integration is chosen such that it satisfies a global accuracy threshold. In our calculation, we use a tolerance of 10^{-20}, which leads to an overall accuracy of 10^{-15} for the real-space Green function. We note that at any given K value in the numerical integration, the Laplace inversion is performed as written in Eq. (20). For $K\leq 2840$, we use the matrix method to compute the eigenvalues (Sec. III A 2). For $K>2840$, we employ the large-K asymptotic expansion (Sec. III A 3) which enhances the efficiency of the calculation; $K=2840$ marks the point where the difference of the first 12 eigenvalues calculated by the matrix method and asymptotic expansion method is less than 10^{-6}.

C. Analytical results for large N

Although our focus thus far is on numerical inversion of the Fourier-Laplace-transformed Green function, it is important to recognize limiting cases where the inversion can be analytically performed. In the large-N limit, the Green function approaches a Gaussian distribution, as dictated by the central limit theorem. Corrections to the Gaussian distribution [7–11] adopt the form of a Gaussian distribution multiplied by a power-series function in R and N^{-1} that approaches unity as $N\to\infty$. This large-N expansion can be derived directly from our continued fraction representation of the Green function in D dimensions [Eq. (19)]. We first rewrite the Green function as

$$G(\vec{K};p) = \frac{1}{P_0+\cfrac{(a_1K)^2}{P_1+\cfrac{(a_2K)^2}{P_2+\cfrac{(a_3K)^2}{\cdots}}}} = \frac{1}{p+\frac{K^2}{D(D-1)(1+A)}} = \sum_{n=0}^{\infty}\frac{1}{\left[p+\frac{K^2}{D(D-1)}\right]^{n+1}}B^n, \tag{34}$$

where

$$A = \frac{p}{D-1} + \frac{\frac{(a_2K)^2}{D-1}}{P_2 + \frac{(a_3K)^2}{P_3 + \frac{(a_4K)^2}{\cdots}}},$$

$$B = \frac{K^2}{D(D-1)} \sum_{n=1}^{\infty} (-1)^{n+1} A^n. \tag{35}$$

These manipulations assume that the relevant contributions occur at small K values, which anticipates the fact that the Gaussian distribution arises from large wavelength contributions; this will be mathematically verified. In the present form, the Fourier-Laplace space Green function appears as an expansion in powers of $[p+\frac{K^2}{D(D-1)}]^{-1}$, leading to poles of increasing order at $p=-K^2/[D(D-1)]$. Singularities at $p=-K^2/[D(D-1)]$ coincide with the small-K asymptotic behavior of the dominant eigenvalue $\mathcal{E}_0=-K^2/[D(D-1)]$ up to the lowest order in K [the next contribution is $\mathcal{O}(K^4)$], as discussed in Sec. III A 1. Although Eq. (34) contains additional singularities within the continued fraction found in B, we can assume the dominant contribution to the inversion is found in the $p=-K^2/[D(D-1)]$ singularities, since the additional singularities have a larger negative real component, driving these contributions to be exponentially small with increasing N. Thus, we expand B in powers of p and K^2, and noting that $p \to -K^2/[D(D-1)]$, we collect terms of order (K^{2n}, p^n) together. Following this procedure and performing the Fourier inversion (see Sec. III B), we arrive at the D-dimensional large-N Green function

$$G(\vec{R};N) = \frac{1}{(2l_p)^D 2^D \pi^{D/2}} \left[\frac{D(D-1)}{N}\right]^{D/2} \exp\left[-\frac{D(D-1)\tilde{r}^2}{4N}\right] \left\{1 - \left[\frac{2D-1}{4(D-1)}\right]\frac{1}{N} - \left[\frac{10-3D-13D^2+28D^3-4D^4}{32(D-1)^2(D+1)(D+2)}\right]\frac{1}{N^2} \right.$$
$$+ \left[\frac{3D-1}{4}\right]\frac{\tilde{r}^2}{N^2} - \left[\frac{4-36D+7D^2+60D^3-5D^4+6D^5}{16D(D-1)(D+1)(D+2)}\right]\frac{\tilde{r}^2}{N^3} - \left[\frac{D(1-5D+4D^2)}{16(D+2)}\right]\frac{\tilde{r}^4}{N^3}$$
$$+ \left[\frac{28-208D+85D^2+449D^3+106D^4+26D^5}{64(D+1)(D+2)^2}\right]\frac{\tilde{r}^4}{N^4}$$
$$\left. - \left[\frac{D(-16+126D-177D^2-215D^3+189D^4+81D^5+12D^6)}{64(D+1)(D+2)^2(D+4)}\right]\frac{\tilde{r}^6}{N^5} + \left[\frac{D^2(1-10D+33D^2-40D^3+16D^4)}{512(D+2)^2}\right]\frac{\tilde{r}^8}{N^6}\right\}, \tag{36}$$

where $\tilde{r}=|\vec{R}|/(2l_p)$. This D-dimensional asymptotic result reduces to expressions found in Refs. [8,11] for three dimensions ($D=3$). This particular asymptotic analysis exploits the fact that the small-K ground-state eigenvalue $\mathcal{E}_0 \approx -K^2/[D(D-1)]$ renders expressions whose Fourier inversion is analytically tractable. However, further refinements in this asymptotic analysis are met with considerable challenges in rendering analytical results in real space. Although it is straightforward to utilize our small-K asymptotic results to render more accurate predictions for $\mathcal{E}_0$ that can be used in the Laplace inversion, the resulting expressions are not easily Fourier inverted to real space. Thus, the Fourier inversion must be performed numerically, exploiting the numerical procedures outlined in the preceding section.

IV. STRUCTURE FACTOR

The physical behavior of a polymer chain is frequently characterized by the single-chain structure factor. The structure factor is directly measured in a scattering experiment, and correlating scattering experiments with theoretical models provides insight into the physical behavior in polymeric fluids [23,52–55]. From a theoretical perspective, the single-chain structure factor acts as an input for treating many-chain systems including concentration fluctuations [56]. Although the structure factors for both a flexible Gaussian chain and a rigid rod are easily expressible, the structure factor of a semiflexible polymer is considerably more difficult to predict theoretically, largely due to the challenges in acquiring analytical expressions for the governing chain statistics. Our goal in this section is to apply our exact results to predict the structure factor for the wormlike chain model that is valid over the entire range of scattering vectors and chain lengths.

We define the structure factor to be

$$S(\vec{k}) = \frac{1}{L^2}\int_0^L ds_1 \int_0^L ds_2 \langle \exp[i\vec{k}\cdot(\vec{r}(s_1)-\vec{r}(s_2))]\rangle, \tag{37}$$

where $\vec{k}$ is the scattering vector, and the angular brackets denote an average with respect to the specific model that governs the chain statistics. Our current manuscript contains exact results that permit the evaluation of the structure factor for the wormlike chain model without excluded volume interactions. Our definition for the structure factor differs from the conventional definition by an extra factor of $1/L$ [57], thus rendering a dimensionless structure factor that tends to one at zero scattering vector.

For the wormlike chain model, the structure factor is given by

$$S(\vec{k}) = \frac{2}{N^2}\mathcal{L}^{-1}\left[\frac{G(K;p)}{p^2}\right], \tag{38}$$

where $K=2l_p|\vec{k}|$, $\mathcal{L}^{-1}$ implies a Laplace inversion from p to $N=L/(2l_p)$, and $G(K;p)$ is the wormlike chain Green function given by Eq. (19). The structure factor is expressible in terms of the magnitude of the scattering vector due to the rotational invariance of the governing statistics. Using results given in Sec. III, we write the structure factor as

$$S(\vec{k}) = \frac{2}{N^2}\left[\frac{N}{j_0^{(+)}(K;0)} - \frac{\partial_p j_0^{(+)}(K;0)}{j_0^{(+)}(K;0)^2} + \sum_{l=0}^{\infty}\frac{\exp(\mathcal{E}_l N)}{\mathcal{E}_l^2 \partial_p j_0^{(+)}(K;\mathcal{E}_l)}\right], \tag{39}$$

where $j_0^{(+)}(K;p)$ and $\partial_p j_0^{(+)}(K;p)$ are continued-fraction functions that are defined in Sec. III (specifically discussed in Sec. III A 6). Equation (39) is evaluated using methods outlined in Sec. III to find the eigenvalues $\mathcal{E}_l$ and to calculate $j_0^{(+)}$ and $\partial_p j_0^{(+)}$. The structure factor given by Eq. (39) is expressed in arbitrary number D dimensions, which is generally useful for treating many-chain systems.

In Ref. [24], we present realizations of the structure factor for the wormlike chain model in three dimensions, demonstrating that our exact results for wormlike chain statistics in three dimensions capture the structure factor over all chain lengths and scattering vectors. Equation (39), along with the techniques provided in Sec. III, provide a convenient methodology for calculating the structure factor as a comparison with scattering experiments. Specifically, the infinite summation in Eq. (39) is truncated at a finite cutoff, and the partial summation is evaluated using methods to evaluate $\mathcal{E}_l$ found in Sec. III. For most calculations, only a couple of terms are necessary to achieve accurate realizations of the structure factor. For example, the structure factor in three dimensions for a chain of length $N=0.1$ requires only four terms in the summation to achieve accuracy within 1.76% difference from a more accurate calculation with 30 terms in the summation (i.e., completely converged in its numerical behavior). Since the terms in the summation decay exponentially with N, larger N values require fewer terms. To illustrate this, we note that the structure factor in three dimensions for a slightly larger chain of length $N=0.5$ calculated with four terms in the summation is within 1.05×10^{-4}% difference from the calculation with 30 terms in the summation. Therefore, most practical applications of Eq. (39) require the inclusion of only a couple of terms in the summation.

We can exploit our asymptotic results from Sec. III and the observations made in the previous paragraph to acquire a simple approximation for the structure factor in three dimensions. For sufficiently large N, the summation in Eq. (39) can be truncated to a single term ($l=0$); this procedure is equivalent to a ground-state dominance approximation. The magnitude of the first term is governed by the value of the ground-state eigenvalue $\mathcal{E}_0$ through the weighting $\exp(\mathcal{E}_0 N)$. Referring to Fig. 1, the ground-state eigenvalue begins at $\mathcal{E}_0=0$ at $K=0$ and then proceeds to $-\infty$ as $K\to\infty$. In Fig. 1, the small-K asymptotic result for $\mathcal{E}_0$ (presented in Sec. III A 1) tracks along the more general matrix-based result for $\mathcal{E}_0$ (presented in Sec. III A 2) up to $K\approx1.89$, where the ground-state eigenvalue is $\mathcal{E}_0=-1.02$. The weighting of the ground-state term at this point is given by $\exp(-1.02N)$, which is negligibly small for large N. We can use the small-K asymptotic results to calculate the structure factor in the large-N limit for all values of K, since the breakdown of the small-K asymptote occurs after the weight of the term is negligibly small.

Combining the concepts outlined in the previous paragraph, we present the large-N limiting behavior of the structure factor for a wormlike chain in three dimensions

$$S^{(LN)}(\vec{k}) = \frac{2}{N^2}\left[\frac{N}{j_0^{(+)}(K;0)} - \frac{\partial_p j_0^{(+)}(K;0)}{j_0^{(+)}(K;0)^2} + \frac{\exp(\mathcal{E}_0^{(SK)}N)}{(\mathcal{E}_0^{(SK)})^2\partial_p j_0^{(+)}(K;\mathcal{E}_0^{(SK)})}\right], \tag{40}$$

where

$$\mathcal{E}_0^{(SK)} = -\frac{1}{6}K^2 - \frac{11}{1080}K^4 - \frac{47}{34020}K^6 \tag{41}$$

is the small-K asymptotic behavior of the ground-state eigenvalue for three dimensions ($D=3$) and $\mu_1=0$ presented in Sec. III A 1 (up to the highest order in our expansion). The large-N approximation of the structure factor is easily evaluated using the methods found in Sec. III A 6 to calculate the continued-fraction functions $j_0^{(+)}$ and $\partial_p j_0^{(+)}$.

Although the large-N structure factor $S^{(LN)}$ is derived assuming large chain lengths N, $S^{(LN)}$ gives accurate values for the structure factor for moderate chain lengths. For example, for $N=6$, comparing $S^{(LN)}$ [Eq. (40)] with the general expression for the structure factor [Eq. (39)] results in a maximum percent difference of less than 1.00% over the entire range of K values. The maximum percent difference decreases with increasing N, such that $N=10$ gives a maximum percent difference of 0.11% and $N=100$ gives a maximum percent difference of 1.17×10^{-4}%. Therefore, the large-N structure factor $S^{(LN)}$ [Eq. (40)] provides reliable values for the wormlike chain structure factor for $N\geq6$ [i.e., less than 1% difference from the exact structure factor found in Eq. (39) over the entire K range]. Since many practical applications of the structure factor involve moderate to large N, the large-N structure factor $S^{(LN)}$ is extremely useful for direct comparison with the results of scattering experiments on semiflexible polymers.

V. DISCUSSION

In Sec. II, we present an exact analytical solution for the Green function in Fourier-Laplace space for a wormlike chain in arbitrary D dimensions. The D-dimensional Green function in Fourier-Laplace space adopts the form of infinite continued fractions, consistent with results for the two- and three-dimensional solutions found in Ref. [24]. Such infinite continued fractions emerge naturally from the diagrammatic methods employed to derive the Green function. Realizations

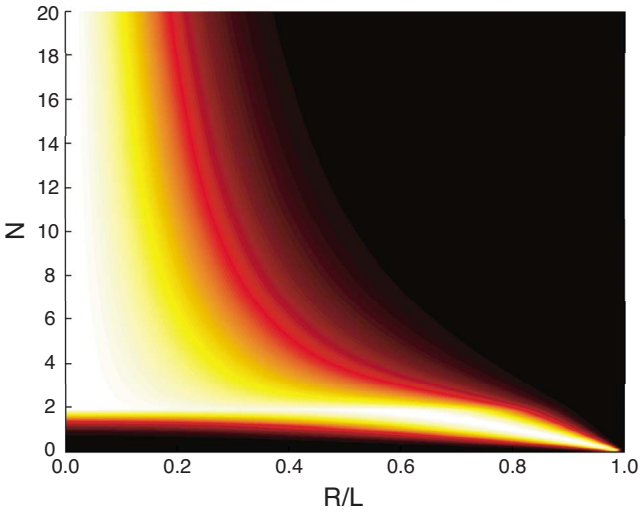

FIG. 2. (Color online) The end distribution function or Green function $G(R;L)$ for the wormlike chain model in three dimensions vs the end extension R/L and the number of Kuhn segments $N=L/(2l_p)$. This surface plot shows high probability in white and low probability in black (see the text for details).

of the chain statistics in real space are rendered upon performing a numerical Fourier-Laplace inversion, as discussed in Sec. III. Owing to these methods, we achieve accurate values of the real-space Green function for chains ranging from rigid to flexible and for all values of end-to-end separation.

Figure 2 shows a birds-eye view of the end distribution function $G(R;L)$ for a wormlike chain in three dimensions. We note that the Green function G only depends on the chain length L and the end-to-end separation R $(R=|\vec{R}|)$ due to rotational invariance. The surface plot shows G versus R/L and the number of Kuhn segments $N=L/(2l_p)$ with white indicating high probability and black indicating low probability. N values range from $N=0$ to $N=20$ with spacing 0.1 between each curve. In order to clearly show the behavior in this surface plot, the Green function G at each N value is divided by its maximum value, thus each rescaled curve runs from zero to one. As such, the color for a given N value in Fig. 2 is black for the smallest value and white for the largest value.

The wormlike chain model exhibits semiflexibility, where the chain appears rigid at small N values and flexible at large N values. The surface plot in Fig. 2 illustrates this physical behavior for a wormlike chain in three dimensions for N values proceeding from small to large. For a chain that is less than one Kuhn segment $[N=L/(2l_p)<1]$, the end statistics are peaked at values near $R/L=1$, indicating the preference for an inflexible chain to remain straight. With increasing length, the peak creeps away from $R/L=1$ due to thermal fluctuations inducing wrinkles in the chain that move the peak in the statistics to smaller end separations. The entropic preference to explore configurational space causes the chain statistics to broaden as N increases. We note that the actual broadening in the chain statistics is much more significant than indicated in Fig. 2, since we plot against R/L rather than R.

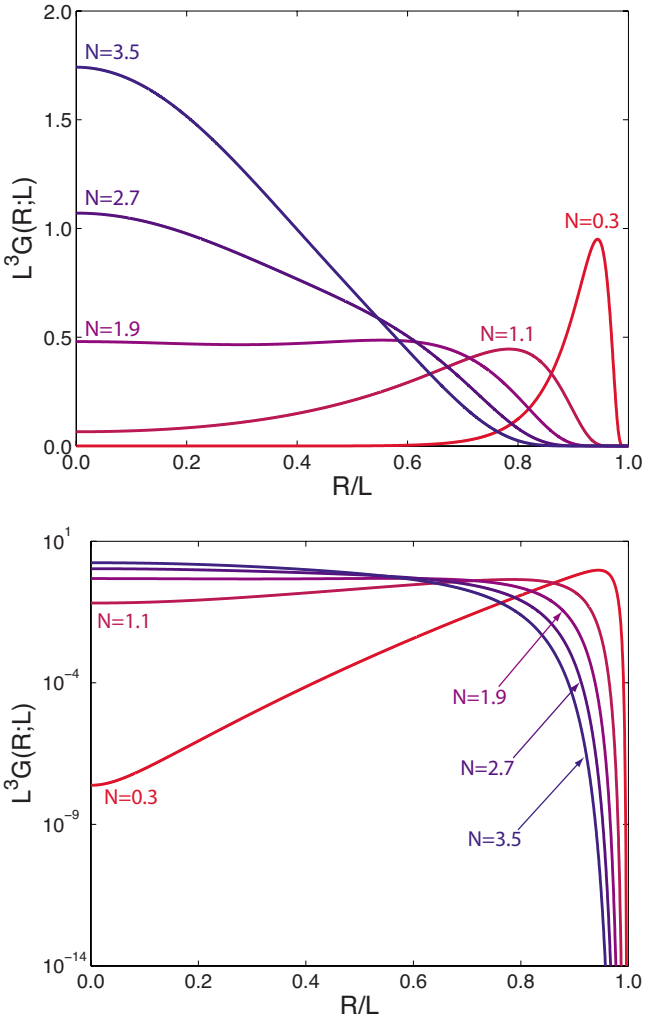

FIG. 3. (Color online) Individual Green function curves for a wormlike chain in three dimensions, extracted from Fig. 2. The chosen N values $(N=0.3,1.1,1.9,2.7,3.5)$ span the transition from rigid to flexible behavior. The top panel gives $L^3G(R;L)$ versus R/L on a linear scale; the same data is given on a logarithmic plot in the bottom panel.

The chain statistics demonstrates a crossover in the physical behavior of the chain proceeding from the peak being pushed away from $R/L=1$ to being located at zero; the crossover between rigid rod and flexible chain occurs at $N\approx 1.9$. Figure 3 shows five individual Green-function curves for a wormlike chain in three dimensions corresponding to $N=0.3$, $N=1.1$, $N=1.9$, $N=2.7$, and $N=3.5$; the top and bottom panels show the Green function on linear and logarithmic scales, respectively. The transition that is evident in Figs. 2 and 3 marks a shift from the chain behaving as a rigid rod to behaving as a flexible thread. Through this transition, the chain statistics exhibit a double-peaked behavior for $N\approx 1.9$, which is included in Fig. 3. This behavior has been demonstrated in several realizations of wormlike chain statistics including the end distribution function with freely rotating ends [25,26] and with a single clamped end [29,58].

The double-peaked behavior coincides with the point where the ring-closure probability of DNA (or J factor) achieves a maximum value [30,59], thus this transition re-

gion is important in the looping probability. Furthermore, the shape of the end distribution function exhibits an almost flat probability versus end extension (i.e., constant free energy of end separation) near $N=1.9$, implying the force opposing looping is nearly zero for such lengths of chain. This may have important consequences on the dynamics of looping segments of chain that are near this length scale. The anomalous physical behavior in this intermediate region is very important since looping plays an important role in the biological function of DNA [60,61].

The accuracy of the numerical Fourier-Laplace inversion is demonstrated in the lower panel of Fig. 3, where we show the Green function on a logarithmic scale. Two regions of R/L tend to be particularly difficult to calculate due to small numerical values of the Green function. For end extensions that are near full extension ($R/L \lesssim 1$), the free energy is dominated by the force required to iron out the thermal wrinkles in the configuration, thus the Green function asymptotically approaches zero in this region for all N values. For end extensions that are near zero ($R/L \gtrsim 0$), the chain must form a loop configuration. Such shapes are energetically prohibitive for rigid or short chains (i.e., $N<1$), leading to small numerical probabilities for $R/L \gtrsim 0$ and $N<1$. These two regions are clearly shown in the lower panel of Fig. 3, where the Green function has values that are many orders of magnitude less than the peak values near unity. Our numerical inversion for this case renders the Green function accurate to $L^3G \approx 10^{-15}$, which is just above machine precision (2.2202×10^{-16} for double precision in MATLAB).

The limiting influence of the machine precision becomes an issue for $N \leq 0.2$ for small end separation ($R/L \gtrsim 0$), where the statistical probabilities are less than the machine precision. As such, the determination of looping probabilities for $N \leq 0.2$ are not accurately determined using our inversion methods. However, we note that the major contribution to the chain statistics are accurately captured at all N values, and our results can be used in problems that do not involve extremely rare events.

The behavior in the limit of full extension is illustrated in Fig. 4, where we plot the Green function (solid curves) versus $1/(1-R/L)$ for the N values found in Fig. 3. As the chain is extended to full extension, the behavior is that of a polymer chain extended in one direction with small perturbations in the transverse directions. There exist $D-1$ transverse directions in D dimensions, e.g., in two dimensions there is one transverse direction. Adopting this view, we perform an analysis of the force-extension behavior (details are not included in this manuscript), which renders an asymptotic form for the Green function near full extension. Upon performing this analysis, we find the asymptotic form of the Green function near full extension for arbitrary dimensions $D \geq 2$ to be

$$G(R;L) \approx C \exp\left[-\frac{(D-1)^2 N}{8(1-R/L)}\right] \tag{42}$$

for $R/L \lesssim 1$, where C is a numerical constant that depends on N and D. There is not a simple governing expression for C since the value must uphold normalization, accounting for the statistical behavior that is outside the asymptotic region. We include the asymptotic limiting behavior [Eq. (42)] in

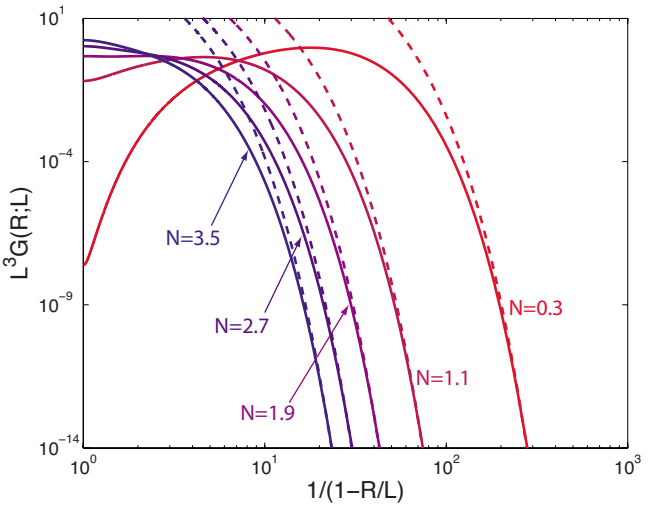

FIG. 4. (Color online) The end distribution function (Green function) for the wormlike chain model in three dimensions vs $1/(1-R/L)$, thus focusing on the behavior near full extension. The asymptotic form presented in Eq. (42) is plotted as dashed curves along with their corresponding Green-function curves (solid curves).

Fig. 4 as the dashed curves, where the numerical value of C is found as a fitting parameter for each N value. The level of accuracy of the Green function permits a direct comparison to the asymptotic form in Eq. (42).

As N proceeds to larger values ($N>1.9$), the chain statistics approach a Gaussian distribution. However, the wormlike chain Green function is only identically Gaussian in the limit $N \to \infty$. The inextensibility constraint for the wormlike chain model prohibits end extensions past $R/L=1$; therefore, the Green function equals zero at full extension. In other words, $G(R/L=1;L)=0$ for all finite N values. This behavior emerges directly from the numerical Fourier-Laplace inversion and is not artificially enforced.

We compare moments of the end distribution function $\langle R_D^{2n} \rangle$ determined using the numerical distribution function presented in Figs. 2–4 and from the exact expressions of the moments derived from the Green function [Eq. (19)]. Our exact results for the Green function found in Eq. (19) act as a generating function for the moments $\langle R_D^{2n} \rangle$, such that

$$\langle R_D^{2n} \rangle = (-1)^n \frac{d^{2n} G(\vec{K};p)}{dK^{2n}}, \tag{43}$$

which requires a Laplace inversion from p to N that is performed analytically. This procedure renders identical results as found using diagrammatic methods found in Refs. [24,30,48,62]. Comparing the numerically determined moments to the exact moments for a wormlike chain in three dimensions, we find a maximum percent difference of 1.61 for the first five moments ($\langle R_D^{2n} \rangle$ for $n=0,1,2,3,4$) over the range $N=0.1-20$. Futhermore, we find excellent agreement between our theoretical results and Monte Carlo simulation results for the end distribution function in three dimensions [13,63] and two dimensions [63] (direct comparison not shown).

Thus far, we focus on the chain statistics for a wormlike chain in three dimensions. The behavior of a polymer chain in arbitrary D dimensions can also be addressed using our exact results. Only two and three dimensions have direct experimental significance; however, the behavior of a wormlike chain in higher dimensions provides a clear understanding of the impact of dimensionality on the statistical behavior. Furthermore, dimensionality plays an important role in understanding the impact of self-interaction on the physical behavior of a polymer chain [31,32,38,41,56,57,64–66].

As previously mentioned, the chain statistics for a wormlike chain exhibits a crossover in the behavior from rigid rod at small N to a flexible chain at large N, e.g., Fig. 3 demonstrates this for three dimensions. This crossover behavior is exhibited in higher dimensions as well, though the N value for the crossover to occur decreases with increasing dimensionality D. In other words, increasing dimensionality causes the chain to become more flexible. Allowing the polymer to explore more dimensions excites conformation fluctuations in the chain due to the entropic desire to access these additional degrees of freedom. This leads to a more flexible chain in higher dimensions.

To demonstrate the impact of dimensionality on chain statistics, we construct a "phase" diagram for the rigid-flexible transition. The Green function gives the free energy $F(R;L)$ for constraining the polymer to have a fixed end separation, such that $F(R;L)=-\ln G(R;L)$. With this interpretation, the rigid-flexible transition with increasing N can be likened to a phase transition.

In Fig. 3, the chain begins at $N=0.3$ with a single peak in the statistics (a single free energy minimum) that is pushed away from the origin ($R/L \lesssim 1$). The chain is in the rigid state at $N=0.3$. With increasing N, the peak creeps toward $R/L=0$ due to the thermal fluctuations causing end retraction. Eventually, a second peak at $R/L=0$ emerges, which marks the introduction of a flexible state at $R/L=0$. The N value that marks the onset of the flexible state N_{FS} also gives the limit of metastability or spinodal point of the flexible state with decreasing N. The rigid state decreases in probability (increases in free energy) with increasing N. Eventually, the probability (or free energy) of the rigid and flexible states become equal; this N value is identified as the rigid-flexible coexistence point N_{RF}. The coexistence point N_{RF} for three dimensions corresponds to $N \approx 1.9$ in Fig. 3. With a further increase in N, the rigid state declines in probability until the probability peak disappears; the N value that marks the limit of metastability of the rigid state is the rigid spinodal point N_{RS}. The rigid-flexible transition is first order in nature because the transition from rigid to flexible behavior is marked by a discontinuity in R/L.

Our thermodynamic picture of the rigid-flexible transition lends insight into the impact of semiflexibility and dimensionality on the physical behavior of a polymer chain. Increasing N can be likened to increasing the temperature, thus the transition from rigid to flexible states is associated with a transition from the energetically preferred state (rigid) to the entropically preferred state (flexible). Since increasing the dimensionality D presents additional degrees of freedom for the polymer to explore, the entropic state (flexible) is preferred with increasing D, thus the rigid-flexible transition occurs at smaller N values at larger D.

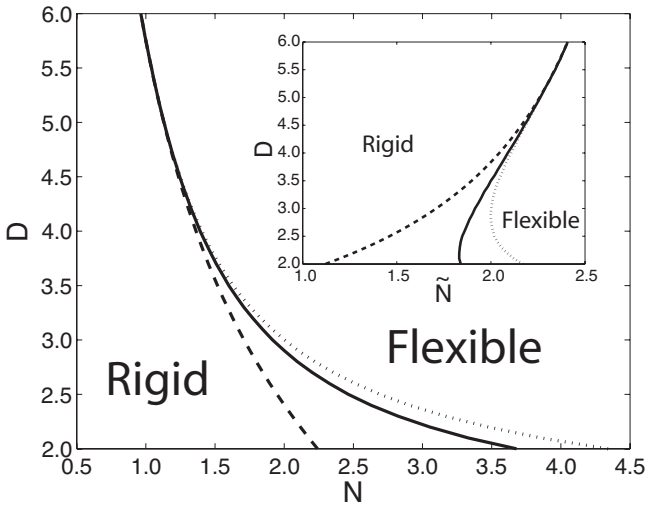

FIG. 5. The rigid-flexible phase diagram for the wormlike chain model showing the chain behavior versus the chain length $N=L/(2l_p)$ and dimensionality D. The transition from rigid to flexible states occurs at N_{RF} (solid curve). The spinodal curves for the rigid state (N_{RS}) and the flexible state (N_{FS}) are the dotted and dashed curves, respectively. These spinodal curves mark the limit of stability of these two states. The inset shows the same phase diagram versus the dimensional chain length $\tilde{N}=(D-1)N/2$ (see the text).

In Fig. 5, we present the phase diagram for the rigid and flexible states versus the number of Kuhn segments $N=L/(2l_p)$ and the dimensionality D. The solid curve in Fig. 5 gives the coexistence point N_{RF} between the rigid and flexible states. The dashed curve gives the spinodal curve for the flexible state N_{FS}, and the dotted curve identifies the spinodal curve for the rigid state N_{RS}. The region between the dashed curve and the solid curve marks conditions where the flexible state is metastable but the rigid state is thermodynamically preferred. Similarly, the region between the solid curve and the dotted curve indicates where the rigid state is metastable but the flexible state is thermodynamically preferred. Figure 5 exhibits a decrease in the rigid-flexible transition N_{RF} with increasing dimensionality D. The spinodal curves asymptotically approach the coexistence curve with increasing D, but the spinodal curves never identically merge. The transition between the rigid and flexible states is consistent with the behavior of a chain with one end clamped in a fixed direction [29].

In the inset of Fig. 5, we plot the phase diagram versus the dimensional chain length $\tilde{N}=(D-1)N/2$. In previous treatments [44–46], the bending deformation energy is scaled by the dimension-dependent bending modulus $(D-1)l_p/2$. The resulting theory renders a Kuhn length $b=2l_p$ that is independent of the dimensionality D. We define $\tilde{N}$ in order to relate our results to these dimension-independent treatments. Upon transforming from $l_p \to (D-1)l_p/2$, the number of Kuhn segments transforms as $L/(2l_p) \to L/[(D-1)l_p]$. Thus, the transformed theory has a number of Kuhn segments $\tilde{N}=L/(2l_p)$, which removes the dimensionality. The inset of Fig. 5 demonstrates that although the impact of dimensionality can be removed from the persistence length (i.e., the Kuhn length), the dimensionality exhibits a nonuniversal impact on the be-

havior of a semiflexible polymer near the rigid-flexible transition (limit of semiflexibility). Although the large chain length behavior tends to a Gaussian with a single statistical length that can be cast in a dimension-independent form, the general behavior of a semiflexible polymer depends on the dimensionality in a nonuniversal manner.

The data plotted in Fig. 5 includes partial dimensionality D (i.e., noninteger values). Analytic continuation of the Green function to partial dimensions is performed directly from Eq. (19). This is not as trivially performed with end-orientation constraint due to the inclusion of the $\boldsymbol{\mu}$ indices in the Green function with orientation constraint. The capacity to extend our results into partial dimensions would be important for an analysis of the influence of self-interaction on the physical behavior of a semiflexible polymer [31,32,38,41,56,57,64–66].

VI. SUMMARY

In this work, we present the exact results for the D-dimensional wormlike chain Green function in Fourier-Laplace space. These results act to generalize our previous results for the behavior in two and three dimensions [24,29], demonstrating that the resulting form is general for all dimensions. Consequently, the present results smoothly interpolate through partial dimensionality, making it possible to determine polymer self-contact perturbatively from the upper critical dimension [31,32,38,41,56,57,64–66]. The resulting expressions for the Green function in Fourier-Laplace space adopt the form of infinite continued fractions, which are attractive both due to their simplicity in implementation and their numerical convergence properties.

The implementation of our results to determine the chain statistics requires a Fourier-Laplace inversion, which is performed numerically. This necessitates a numerical scheme that accurately performs the inversion up to a desired degree of accuracy, noting the lower bound on the accuracy associated with the machine precision. We separately address the Laplace and Fourier inversions in order to explicitly give a set of tools for achieving accurate inversions.

For the Laplace inversion, the major hurdle lies in the calculation of the poles (or eigenvalues) of the continued fraction. We present three methods for pole evaluation that are accurate at small, intermediate, and large frequencies K. The small-K asymptotic expansion gives accurate poles up to $K \approx 1$, thus there is a small window of utility for this technique. The intermediate-K method determines the poles as the eigenvalues of the scattering matrix. This technique is accurate and convenient for both the small-K and intermediate-K determination of the poles. However, the intermediate-K matrix method exhibits instabilities with increasing K; thus, there exists a need for a separate large-K method. To this end, we utilize Rayleigh-Schrödinger perturbation theory to give an asymptotic expansion that accurately determines the poles in the large-K limit. These three methods provide a framework for the accurate determination of the poles over all frequency values. The frequency integration involved in the Fourier inversion is performed numerically such that the Laplace inversion must be performed at each K step in the numerical integration. Therefore, the Laplace inversion must be performed efficiently and accurately at each K step.

We then proceed to present a simple methodology for evaluating the single-chain structure factor, which plays an important role as a direct comparison to scattering experiments and as a necessary input to studying many-chain systems. First, we provide a general methodology for evaluating the structure factor that is valid over the entire range of chain lengths and scattering vectors. We then proceed to present a simple, closed-form expression for the structure factor that is accurate for moderate to large chain length ($N > 6$).

With the methods that we develop for the Fourier-Laplace inversions, we present realizations of the end distribution function for the wormlike chain model. Our results in three dimensions demonstrate accuracy up to the machine-precision limit for all values of the number of Kuhn segments N. Increasing dimensionality tends to cause the chain to become more flexible due to the additional degrees of freedom that are presented to the chain. The entropic desire for the chain to explore these additional degrees of freedom introduces conformation wrinkles in the chain, thus enhancing the flexibility. This general trend is demonstrated in a phase diagram for the transition from the chain behaving as a rigid rod at small N values to behaving as a flexible thread at large N values. The rigid-flexible transition is first order in nature, reflecting the double-peaked shape of the end distribution function that was previously reported [25,26,29].

The techniques presented in this work enable the accurate evaluation of the end distribution function for the wormlike chain model. These methods provide a framework that permits the evaluation of the chain statistics over chain lengths ranging from rigid to flexible. Therefore, these methods can be applied to a wide range of problems involving semiflexible polymers.

ACKNOWLEDGMENTS

The authors gratefully acknowledge helpful discussions with Zhen-Gang Wang. Elena F. Koslover acknowledges funding support from the Fannie and John Hertz Foundation and from the National Science Foundation.

APPENDIX

We consider the partition function of a wormlike chain subject to a tensile force $\vec{f}$ acting on the end-to-end distance vector $\vec{R} = \int_0^L ds\vec{u}$ in D dimensions. In Eq. (7), the external Hamiltonian that arises from this tensile force is $\beta\mathcal{H}_{\text{ext}} = -\beta\vec{f}\cdot\int_0^L ds\vec{u}$ [note, $\beta = 1/(k_B T)$]. Without loss of generality, we assume the force to be aligned along the x_D axis. Comparing aforementioned $\beta\mathcal{H}_{\text{ext}}$ with that of Eq. (7) demonstrates that we must replace $\vec{k}$ with $-i\vec{f}$ (and K with $-iF$) in Eqs. (7) and (19), where $\vec{F} = 2l_p\vec{f}/(k_B T)$. Hence, according to Eq. (19), the Laplace-transformed partition function $q(\vec{F};p)$ in D dimensions adopts the form of the infinite continued fraction

$$q(\vec{F};p) = \frac{1}{P_0 - \dfrac{(a_1F)^2}{P_1 - \dfrac{(a_2F)^2}{P_2 - \dfrac{(a_3F)^2}{\cdots}}}}, \tag{A1}$$

where p is the Laplace variable conjugated with $N=L/(2l_p)$, $P_\lambda = p+\lambda(\lambda+D-2)$, and $a_\lambda = [\frac{\lambda(\lambda+D-3)}{(2\lambda+D-2)(2\lambda+D-4)}]^{1/2}$. To retrieve the partition function in real space, we must invert the Laplace transform in Eq. (A1). Accurate inversion of the Laplace transform requires accurate evaluation of the poles or eigenvalues, as in the inversion of the Green function [Eq. (19)]. We adopt the same procedure as discussed in Sec. III, thus dividing the force spectrum into three regimes: small F, intermediate F, and large F. Here, we briefly discuss the minor alterations that must be performed to the methods present in Sec. III to accurately perform the Laplace inversion for a wormlike chain under external tension.

1. Eigenvalue evaluation (small-F regime)

As in Sec. III A 1, the small-F asymptotic behavior of the eigenvalue $\mathcal{V}_l$ (analogous to $\mathcal{E}_l$ found in Sec. III) behaves as a power-law expansion in powers of F^2, written as $\mathcal{V}_l = \Sigma_{n=0}^{\infty} h_{2n}^{(l)} F^{2n}$. We write the governing continued fraction for $\mathcal{V}_l$ using Eq. (21), replacing K with $-iF$. Following an identical procedure as discussed in Sec. III A 1, we arrive at the expansion coefficients $h_{2n}^{(l)} = (-1)^n b_{2n}^{(l)}$, where $b_{2n}^{(l)}$ are tabulated in Table I.

2. Eigenvalue evaluation (intermediate-F regime)

With increasing F, the small-F power-law expansion is no longer valid. To compute the eigenvalues, we utilize the numerical matrix method employed in Sec. III A 2 replacing K with $-iF$. Upon performing this transformation, the governing matrix ($\mathbf{J}^{(0)}$) is Hermitian, thus the eigenvalues are all real. As in Sec. III A 2, the infinite matrix is truncated at a finite level that is sufficiently large to achieve accuracy in the numerical inversion. As a rule of thumb, we find accuracy in the first n eigenvalues when we set the cutoff to the matrix to $n_{\text{cutoff}} = 4n$.

3. Eigenvalue evaluation (large-F regime)

Due to numerical instability in using the above-mentioned matrix method for large F values, we adapt the perturbation procedure discussed in Sec. III A 3 to accurately determine the eigenvalues $\mathcal{V}_l$ in the large-F limit. Replacing K with $-iF$ in Eq. (22), the Schrödinger equation [Eq. (22)] becomes

TABLE III. Large-F asymptotic expansion coefficients for $\mathcal{V}_l$.

In these expressions: $m=\mu_1+\frac{D-3}{2}$; $s=2l+m+1$; $l=0,1,2,3,\ldots$

$V_0^{(l)} = \frac{1}{2}s$

$V_1^{(l)} = -\frac{1}{8}(s^2+3-3m^2) - m(m+1)$

$V_2^{(l)} = -\frac{1}{32}s(s^2+3-9m^2)$

$V_3^{(l)} = -\frac{1}{256}[(5s^4+34s^2+9) - (102s^2+42)m^2 + 33m^4]$

$V_4^{(l)} = -\frac{1}{2048}s[(33s^4+410s^2+405) - (1230s^2+1722)m^2 + 813m^4]$

$V_5^{(l)} = -\frac{9}{4096}[(7s^6+140s^4+327s^2+54) - (420s^4+1350s^2+286)m^2 + (495s^2+314)m^4 - 82m^6]$

$$(\tilde{\nabla}_D^2 + F\cos\theta_{D-2})\psi_l = \mathcal{V}_l\psi_l, \tag{A2}$$

where ψ_l and $\mathcal{V}_l$ are eigenfunctions and eigenvalues, respectively, and the angular Laplacian $\tilde{\nabla}_D^2$ is given by Eq. (23). Following the same procedure as in Sec. III A 3, we define the perturbation parameter $\alpha = 1/\sqrt{8F}$ and the variable $x = \alpha^{-1}\sin^2(\theta_{D-2}/2)$, with a range from zero to $\sqrt{8F}$ that approaches infinity as $F\to\infty$. Using these transformations in Eq. (A2), we now have the effective eigenvalue problem

$$(\mathcal{H}_0 + \alpha\mathcal{H}')\Phi_l = \eta_l\Phi_l, \tag{A3}$$

where the effective eigenvalue η_l and the original eigenvalue $\mathcal{V}_l$ have the following relation:

$$\mathcal{V}_l = F - \mu_1(\mu_1+D-2) - \frac{1}{\alpha}\eta_l. \tag{A4}$$

The ground-state Hamiltonian operator is $\mathcal{H}_0 = -x\frac{d^2}{dx^2} - (\mu_1 + 1 + \frac{D-3}{2})\frac{d}{dx} + \frac{x}{4}$, and the perturbing Hamiltonian operator is $\mathcal{H}' = x^2\frac{d^2}{dx^2} + 2(\mu_1+1+\frac{D-3}{2})x\frac{d}{dx}$. Now, Rayleigh-Schrödinger perturbation theory is applied [51], which renders an expansion of Φ_l and η_l in powers of α. Namely,

$$\mathcal{V}_l = F - \mu_1(\mu_1+D-2) - \frac{1}{\alpha}\sum_{n=0}^{\infty}\alpha^n V_n^{(l)}. \tag{A5}$$

Table III contains the large-F expansion coefficients $V_l^{(n)}$ up to $n=5$ (order F^{-2} contribution to $\mathcal{V}_l$).

[1] O. Kratky and G. Porod, Recl. Trav. Chim. Pays-Bas **68**, 1106 (1949).

[2] N. Saito, K. Takahash, and Y. Yunoki, J. Phys. Soc. Jpn. **22**, 219 (1967).

[3] L. D. Landau and E. M. Lifshitz, *Theory of Elasticity* (Pergamon, New York, 1986).

[4] A. E. H. Love, *A Treatise on the Mathematical Theory of Elasticity* (Dover, New York, 1944).

[5] J. F. Marko and E. D. Siggia, Macromolecules **28**, 8759 (1995).

[6] J. D. Moroz and P. Nelson, Macromolecules **31**, 6333 (1998).

[7] H. E. Daniels, Proc. R. Soc. Edinburgh, Sect. A: Math. Phys.

Sci. **63**, 29 (1952).
[8] W. Gobush, W. H. Stockmayer, H. Yamakawa, and W. S. Magee, J. Chem. Phys. **57**, 2839 (1972).
[9] H. Kleinert, *Path Integrals in Quantum Mechanics, Statistics, Polymer Physics, and Financial Markets* (World Scientific, Singapore, 2004).
[10] J. Shimada, M. Fujii, and H. Yamakawa, J. Polym. Sci. Part A-2 **12**, 2075 (1974).
[11] F. F. Semeriyanov and S. Stepanow, Phys. Rev. E **75**, 061801 (2007).
[12] H. Yamakawa and M. Fujii, J. Chem. Phys. **59**, 6641 (1973).
[13] J. Wilhelm and E. Frey, Phys. Rev. Lett. **77**, 2581 (1996).
[14] R. A. Harris and J. E. Hearst, J. Chem. Phys. **44**, 2595 (1966).
[15] Y. Tagami, Macromolecules **2**, 8 (1969).
[16] K. F. Freed, J. Chem. Phys. **54**, 1453 (1971).
[17] M. G. Bawendi and K. F. Freed, J. Chem. Phys. **83**, 2491 (1985).
[18] J. B. Lagowski, J. Noolandi, and B. Nickel, J. Chem. Phys. **95**, 1266 (1991).
[19] R. G. Winkler, P. Reineker, and L. Harnau, J. Chem. Phys. **101**, 8119 (1994).
[20] R. G. Winkler, L. Harnau, and P. Reineker, Macromol. Theory Simul. **6**, 1007 (1997).
[21] A. L. Kholodenko, Ann. Phys. **202**, 186 (1990).
[22] A. L. Kholodenko, J. Chem. Phys. **96**, 700 (1992).
[23] D. Potschke, P. Hickl, M. Ballauff, P. O. Astrand, and J. S. Pedersen, Macromol. Theory Simul. **9**, 345 (2000).
[24] A. J. Spakowitz and Z.-G. Wang, Macromolecules **37**, 5814 (2004).
[25] J. Samuel and S. Sinha, Phys. Rev. E **66**, 050801 (2002).
[26] J. Samuel and S. Sinha, Phys. Rev. Lett. **90**, 098305 (2003).
[27] S. Stepanow and G. M. Schütz, Europhys. Lett. **60**, 546 (2002).
[28] H. N. V. Temperley and E. H. Lieb, Proc. R. Soc. London, Ser. A **322**, 251 (1971).
[29] A. J. Spakowitz and Z.-G. Wang, Phys. Rev. E **72**, 041802 (2005).
[30] A. J. Spakowitz, Europhys. Lett. **73**, 684 (2006).
[31] P. J. Flory, *Principles of Polymer Chemistry* (Cornell University Press, Ithaca, 1953).
[32] P.-G. de Gennes, *Scaling Concepts in Polymer Physics* (Cornell University Press, Ithaca, 1979).
[33] H. Yamakawa, *Modern Theory of Polymer Solutions* (Harper and Row, New York, 1971).
[34] M. Muthukumar and B. G. Nickel, J. Chem. Phys. **80**, 5839 (1984).
[35] K. F. Freed, *Renormalization Group Theory of Macromolecules* (John Wiley & Sons, New York, 1987).
[36] R. Podgornik, Phys. Rev. E **70**, 031801 (2004).
[37] R. Podgornik, P. L. Hansen, and V. A. Parsegian, J. Chem. Phys. **113**, 9343 (2000).
[38] P. L. Hansen, D. Svensek, V. A. Parsegian, and R. Podgornik, Phys. Rev. E **60**, 1956 (1999).
[39] P. L. Hansen and R. Podgornik, J. Chem. Phys. **114**, 8637 (2001).
[40] M. G. Bawendi and K. F. Freed, J. Chem. Phys. **86**, 3720 (1987).
[41] Z. Y. Chen and J. Noolandi, J. Chem. Phys. **96**, 1540 (1992).
[42] M. Pretti, Phys. Rev. E **66**, 061802 (2002).
[43] Z. Y. Wen and J. Avery, J. Math. Phys. **26**, 396 (1985).
[44] P. Benetatos and E. Frey, Phys. Rev. E **70**, 051806 (2004).
[45] H. Kleinert and A. Chervyakov, J. Phys. A **39**, 8231 (2006).
[46] D. Chaudhuri, Phys. Rev. E **75**, 021803 (2007).
[47] R. P. Feynman and A. R. Hibbs, *Quantum Mechanics and Path Integrals* (McGraw-Hill, New York, 1965).
[48] H. Yamakawa, *Helical Wormlike Chains in Polymer Solutions* (Springer-Verlag, Berlin, 1997).
[49] C. Flammer, *Spheroidal Wave Functions* (Stanford University Press, Stanford, 1957).
[50] H. S. Wall, *Analytic Theory of Continued Fractions* (Chelsea Publishing Company, New York, 1957).
[51] M. Cohen and T. Feldmann, J. Phys. B **15**, 2563 (1982).
[52] L. Cannavacciuolo, J. S. Pedersen, and P. Schurtenberger, Langmuir **18**, 2922 (2002).
[53] J. S. Pedersen and P. Schurtenberger, J. Polym. Sci., Part A-2 **42**, 3081 (2004).
[54] J. S. Pedersen, M. Laso, and P. Schurtenberger, Phys. Rev. E **54**, R5917 (1996).
[55] C. Svaneborg and J. S. Pedersen, Curr. Opin. Colloid Interface Sci. **8**, 507 (2004).
[56] Z.-G. Wang, J. Chem. Phys. **117**, 481 (2002).
[57] M. Doi and S. F. Edwards, *The Theory of Polymer Dynamics* (Oxford University Press Inc., New York, 1986).
[58] P. Benetatos, T. Munk, and E. Frey, Phys. Rev. E **72** 030801 (2005).
[59] J. Shimada and H. Yamakawa, Macromolecules **17**, 689 (1984).
[60] J. Müller, S. Oehler, and B. Müller-Hill, J. Mol. Biol. **257**, 21 (1996).
[61] L. Finzi and J. Gelles, Science **267**, 378 (1995).
[62] A. J. Spakowitz and Z.-G. Wang, J. Chem. Phys. **119**, 13113 (2003).
[63] A. Dhar and D. Chaudhuri, Phys. Rev. Lett. **89**, 065502 (2002).
[64] M. K. Kosmas and K. F. Freed, J. Chem. Phys. **69**, 3647 (1978).
[65] Y. Oono, T. Ohta, and K. F. Freed, J. Chem. Phys. **74**, 6458 (1981).
[66] Z.-G. Wang, A. M. Nemirovsky, and K. F. Freed, J. Chem. Phys. **85**, 3068 (1986).